ABSTRACT

WILBERDING, KATHRYN. Investigations of Structure Property Relationships of Heterometallic Hybrids and ABO_3 Perovskites. (Under the direction of Prof. Paul A. Maggard).

New sources of renewable fuels and energy are becoming ever prevalent in the global economy as fossil fuel technologies suffer diminishing reserves and negatively affect the environment. Sunlight based renewable energies have been of great of interest over the past few decades because the solar spectrum contains enough energy to satisfy the global energy demand. Two critical components of sunlight driven energy technologies are visible-light absorption and charge mobility because without effective charge mobility the electron-hole pairs can become trapped and recombine preventing the charge carriers from being able to oxidize and/or reduce water. Research described herein has fallen into two main areas: 1) Ruthenium inorganic/organic hybrids for visible-light absorption and 2) perovskite $BaSnO_3$ and $PbTiO_3$ particles for their high charge mobility property.

In the first area, the syntheses of Ru(II)/Nb(V) and Ru(II)/V(V) hybrids were attempted and resulted in the discovery of $[Ru(C_{10}H_8N_2)_3][NbF_6]_2$ (**I**) and $[Ru(C_{10}H_8N_2)_2(CO)Cl][V_2(C_2O_4)_3O_2(H_2O)]_{0.5} \cdot H_2O$ (**II**). Each hybrid crystal structure was solved and refined. The lowest energy optical transition for each crystal was measured by UV-Vis diffuse reflectance and converted to absorption using the Kubelka-Munk transformation. The lowest energy optical transition is at 2.15 eV and 2.54 eV for **I** and **II** respectively. Relative to the energies of the lowest energy optical transitions of parent ruthenium bipyridine complexes, the absorption spectra of both **I** and **II** undergo a blue shift in the absorption spectra. Both **I** and **II** have optical transitions small enough to absorb in the visible range.

In the second area, two ABO_3 perovskites, $BaSnO_3$ and $PbTiO_3$, were investigated for their photoelectrochemical and photocatalytic properties. Electronic structure calculations band dispersion that can yield high charge mobility. However, previous investigations in the literature showed small photoresponses and photocatalytic activities. Therefore, enhancement of the photoelectrochemical and photocatalytic properties of each perovskite was attempted by *n*-type doping of La^{3+} cations to the A site and measuring the effect on the photoresponse and O_2 evolution activity. A previously unreported synthetic approach for the formation of La-doped $BaSnO_3$ is included. Phase pure products of $BaSnO_3$ and $PbTiO_3$ were confirmed by powder X-ray diffraction and band gap sizes were measured by UV-Vis diffuse reflectance. Photoelectrochemical and photocatalytic responses of both non-doped and La-doped $BaSnO_3$ and $PbTiO_3$ were measured. The La-doped $BaSnO_3$ series demonstrated a reduction in both photoresponse as well as photocatalytic oxidation ability upon higher doping concentration. Likewise $PbTiO_3$ demonstrated a reduction in both photoresponse as well as photocatalytic oxidation ability upon doping with La^{3+} cations.

Investigations of Structure Property Relationships of Heterometallic Hybrids and ABO_3 Perovskites

by
Kathryn Lynn Wilberding

A thesis submitted to the Graduate Faculty of
North Carolina State University
in partial fulfillment of the
requirements for the degree of
Master of Science

Chemistry

Raleigh, North Carolina

2014

APPROVED BY:

_____	_____
Paul A. Maggard Committee Chair	David A. Shultz
_____	
Walter W. Weare	

DEDICATION

This work is dedicated to my entire family and all my friends for all of their love, support, encouragement, and faith in me throughout my life. Without their love and support I wouldn't be where I am today. Thank you.

BIOGRAPHY

Kathryn Wilberding was born in El Paso, Texas in 1987. She graduated from Woodinville High School in May 2006 and went onto the University of New Haven in West Haven, Connecticut. In the summer of 2009 she joined both Cwiklik and Associates and KMS Forensics for simultaneous, but separate research projects in the field of Forensic Science. With Cwiklik and Associates she studied the microscopic products formed from the pyrolysis of cotton fabrics and received the National Institute of Justice and Forensic Science Foundations' Forensic Science Student Research Program award to present their research findings at the American Academy of Forensic Science at the society's annual meeting in February 2010. Kathryn double majored, completing a Bachelor of Science in Forensic Science and a Bachelor of Science in Chemistry in May 2010. She then joined Dr. Paul A. Maggard's research group at North Carolina State University in the Fall of 2010 where she has worked on the structure property relations of heterometallic hybrids and wide band gap semiconductors with specific emphasis on the photocatalytic properties of synthesized materials.

ACKNOWLEDGMENTS

I would like to thank my advisor, Dr. Paul A. Maggard, who has helped me to discover what I wish for my career to become through his careful guidance of my work, his patience and his understanding. I would also like to thank my committee members, Dr. Paul Maggard, Dr. David Shultz and Dr. Walter Weare for their advice and input.

I would like to thank my group members, Nacole, Lan, Jonathan, Ian, Brandon, David, and Zahir, for all of their assistance in helping me to understand my research. I would also like to thank former group members, Dr. Prangya Sahoo and Dr. Lindsay Fuoco, for all of their instruction and suggestions. Thank you to Paul Boyle for collecting single crystal data for me and helping me start solving new structures. Thank you to Roger Sommer for assisting me with single crystal solving and refining software and all the input on solving my crystal structures.

Finally I would like to thank all my teachers and mentors for helping me to become a better scientist and a better student of life.

TABLE OF CONTENTS

LIST OF TABLES

CHAPTER 3

LIST OF FIGURES

CHAPTER 1

CHAPTER 2

CHAPTER 3

CHAPTER 4

PART 1

INTRODUCTION

CHAPTER 1

OVERVIEW

Research into new semiconductor materials has garnered significant and varied interest across the fields of science. In chemistry, semiconductor materials have been investigated for everything from switches to photocatalysts.[3] In the area of photocatalysts, semiconductor materials have been intensely investigated because the need for clean renewable energy sources has arisen as finite sources of energy such as oil and natural gas have increased in costs both financially and environmentally.[4-6] With advances in our understanding of photocatalytic water reduction made by Fujishima and Honda in 1972, as well as the development of the Grätzel cell, intensive investigations into the use of semiconductors as photocatalysts, and scaffolds for dye sensitized solar cells have been reported.[7-11] However, as the ideal photocatalyst is yet to be discovered, continued research in the area of photocatalytic water splitting and the necessary conditions to achieve high efficiencies is still ongoing.

Photoelectrochemistry of films and photocatalysis of suspended particles have received considerable attention in the literature as two ways to convert solar energy into either electrical energy or chemical fuels.[8,12-14] Photocatalytic oxidation and/or reduction of water to produce O_2 and/or H_2 has been a long-standing challenge. Photocatalytic water splitting in general requires the light induced excitation of electrons from the valence band of an extended solid across the band gap to the conduction band, thereby producing an electron-hole pair.[15] More specifically, photons cause electrons in the valence band of a semiconducting material to be excited to the conduction band of that material. In molecules

photons excite electrons from the highest occupied molecular orbital (HOMO) to the lowest unoccupied molecular orbital (LUMO). At the surface of metal oxides in solution, the band bending facilitates the electron-hole separation toward the surface/electrolyte interfaces.[16-18] In *p*-type metal oxides the electrons move into the electrolyte because the valence and conduction bands bend downward. In *n*-type metal oxides, the electrons move into the bulk because the bands bend up (Figure 1.1). Thus, in *n*-type metal oxides electrons move away from the surface of the material where they can either go through a circuit as in a photoelectrochemical cell to a counter electrode, where the electrons can reduce H_2O to H_2.[19] The holes, the minority carriers, move to the surface of the metal oxide and oxidize H_2O to O_2 if the valence band is at a potential more positive than 1.23 V versus NHE.[1] For total water splitting, $H_2O + 2h\nu \rightarrow H_2 + \frac{1}{2}O_2$, the conduction band of the metal oxide needs to be at a more negative potential than the reduction of water to H_2 (0 V versus NHE) and the valence band of the metal oxide must be at a more positive potential than the oxidation of water to O_2 (1.23 V versus NHE) (Figure 1.2).[1]

Beyond the valence and conduction band energies of a material, the band gap size is also important. In order for the semiconductor to absorb an appropriate range of visible-light energies, the band gap should be around 1.8 eV. The ideal visible-light photocatalyst will have a band gap below 2.0 eV with a valence band positioned at a more positive potential to water oxidation and a conduction band positioned at a more negative potential to water reduction. One promising approach to develop visible-light absorbing photocatalysts is with the use of heterometallic metal organic frameworks.

Metal-organic frameworks are crystalline hybrid materials that form by linking inorganic metal-oxide components through organic ligands to form extended solids.[20,21] Such materials have received growing interest for their potential fine molecular level structure control as well as their ability as multifunctional materials.[22-25] For instance, metal organic vanadates and molybdates have a number of structures dictated by the organic ligand that may be used in fields such as catalysis, gas absorption, electrical conductivity, and optical absorption.[26,27] Specifically, previous work in the Maggard group includes the synthesis and characterization of hybrids such as $M(pyz)V_4O_{10}$ (M=Co, Ni, Zn) (pyz = pyrazine) and $M(pzc)_2(H_2O)AgReO_4$ (M = Cu, Ni, Co) (pzc = pyrazine-2-carboxylate).[26,28,29] All of these studies have shown that metal oxide organic hybrid systems are promising photocatalytic materials because of the combination of the robust nature and electronic properties of the metal oxides with the versatility and chemical flexibility of organic components. Furthermore, previous work by the Maggard group has specifically shown that metal oxide combinations of d^0 and d^{10} transition metals, such as Ta^{5+} and Nb^{5+} with Cu^+, could yield hybrid compounds with lower band gap sizes for the absorption of visible-light.[30] One direction of continued research interest has been to incorporate transition metals known to be robust photocatalysts under photocatalytic conditions, such as containing the Ru^{2+} cation.[31-33] Ru(II)-polypyridyl complexes have long been investigated as molecular dyes for dye sensitized solar cells and photocatalysis.[11,34] However, relatively few heterometallic catalysts containing ruthenium are known.[35-37] Thus my research efforts in this area have focused on the synthesis and characterization of new visible-light-absorbing hybrids containing ruthenium as potential photocatalysts.

While visible-light absorption is a critical property of a good photocatalyst, other properties such high charge mobility, high surface areas, and high crystallinity are also important for an ideal photocatalyst, because without these characteristics the energy absorbed would not be efficiently utilized. For example, if a visible-light-absorbing material has poor conductivity (such as from poor charge mobility) then much of the energy absorbed would be lost to recombination. One of the many obstacles in developing the ideal photocatalyst or photocatalytic system has been recombination of the electron-hole pair. Poor charge separation can arise from a few factors including, but not limited to: 1) relatively small band bending causing electrons and holes to take longer to move away from each other than it takes for the pair to recombine, 2) electrons and/or holes recombine with holes and/or electrons from defects in the crystal lattice 3) the inherent mobility of the majority carriers is low (from low band dispersion) leading to low conductivity.[5,19] Investigating solutions to each of these obstacles can help improve upon the design of photocatalysts or photocatalytic systems.

Semiconducting metal oxides have a large variety of possible compositions and structures and a wide range of chemical and physical properties.[17,18] For example, the electronic properties can range from metallic (ReO_3) to semiconducting (ZnO) to insulating ($BaTiO_3$).[38-40] Furthermore, metal oxides are the primary components of many porous-based materials such as metal organic frameworks, which have been used in ion exchange gas absorption, and catalytic reactions.[24,25,41] Much of the recent work in this area has focused on the synthesis of metal-oxide photoelectrodes and photocatalysts capable of absorbing visible-light to oxidize or reduce water for fuels.[42,43] Metal oxides have also been investigated as

scaffold materials for dye-sensitized solar cells because they are relatively robust against photocorrosion and provide pathways for charge carrier transport.[44-46] There are two types of semiconducting metal oxides: *n*-type (where the majority carriers are negatively charged, electrons) and *p*-type (where the majority carriers are positively charged, holes). Of the *n*-type semiconductor metal oxides currently known only a small number are known to be visible-light active (e.g. $BiVO_4$ and WO_3).[43,47] Most *n*-type metal oxides like TiO_2 and $BaSnO_3$ are only UV light active.[14,48-50] Thus for this research visible-light absorption was not a requirement for the *n*-type metal oxides investigated.

The research herein focused on addressing both poor charge transfer character and low charge carrier concentration by using a semiconducting metal oxide with inherent high charge mobility character, as indicated by electron structure calculations, and increasing the charge carrier concentration through doping. ABO_3 perovskites are one class of metal oxides in which a few members of the $ASnO_3$ sub-class have previously shown photoelectrochemical and photocatalytic responses.[48,49,51] Studies of the photoelectrochemical properties found the response was improved by producing an ideal cubic perovskite structure when Ba^{2+} cations are located at the A site, or by creating oxygen vacancies such as in $BaSnO_{3-\delta}$.[48,51] Increasing the cation size created the ideal cubic perovskite structure $BaSnO_3$ because the Ba^{2+} cation size resulted in a Sn-O-Sn bond angle of 180°. At 180° the s and p orbitals of Sn and O fully overlap resulting in higher conductivity and ultimately in higher O_2 production than $CaSnO_3$ or $SrSnO_3$, which have distorted structures. Furthermore, the reported electronic structure calculations of $CaSnO_3$, $SrSnO_3$, and $BaSnO_3$ indicate $BaSnO_3$ has inherent high charge mobility.[49] Despite the inherent

mobility characteristic, $BaSnO_3$ has shown minimal photoelectrochemical and photocatalytic likely due to its large band gap size making it only UV active. One approach to improving the photoelectrochemical response of $BaSnO_3$ which has been reported, involved *n*-type doping of the $BaSnO_3$ structure with La^{3+} cations at the A site to increase the number of charge carriers.[52-54] What has not been investigated is the photocatalytic activity that results from doping La^{3+} cations into the A site of $BaSnO_3$.

The specific goal of the research presented herein was to better understand, a) optical property and structure relationships through the targeted synthesis and characterization of new heterometallic hybrids containing ruthenium and, b) the effect on photocatalytic activity of La-doping into $BaSnO_3$ and $PbTiO_3$ for increased charge carrier concentration.

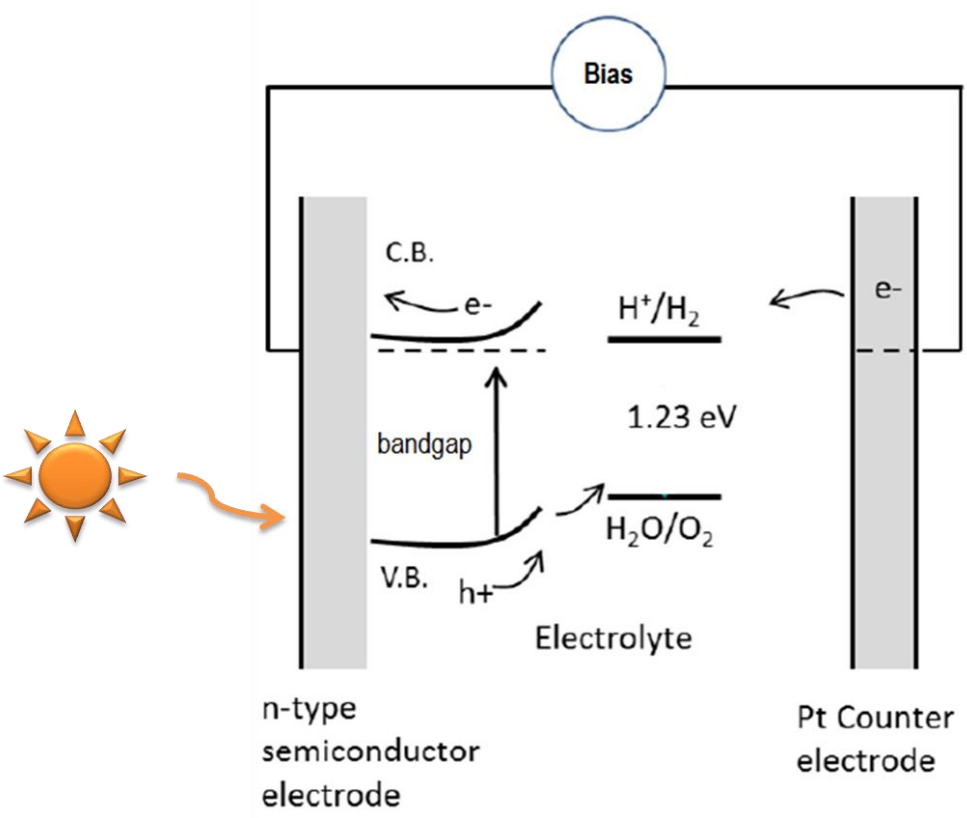

Figure 1.1: PEC cell configuration of an *n*-type semiconductor electrode with a Pt counter electrode. Image adapted from reference 1.

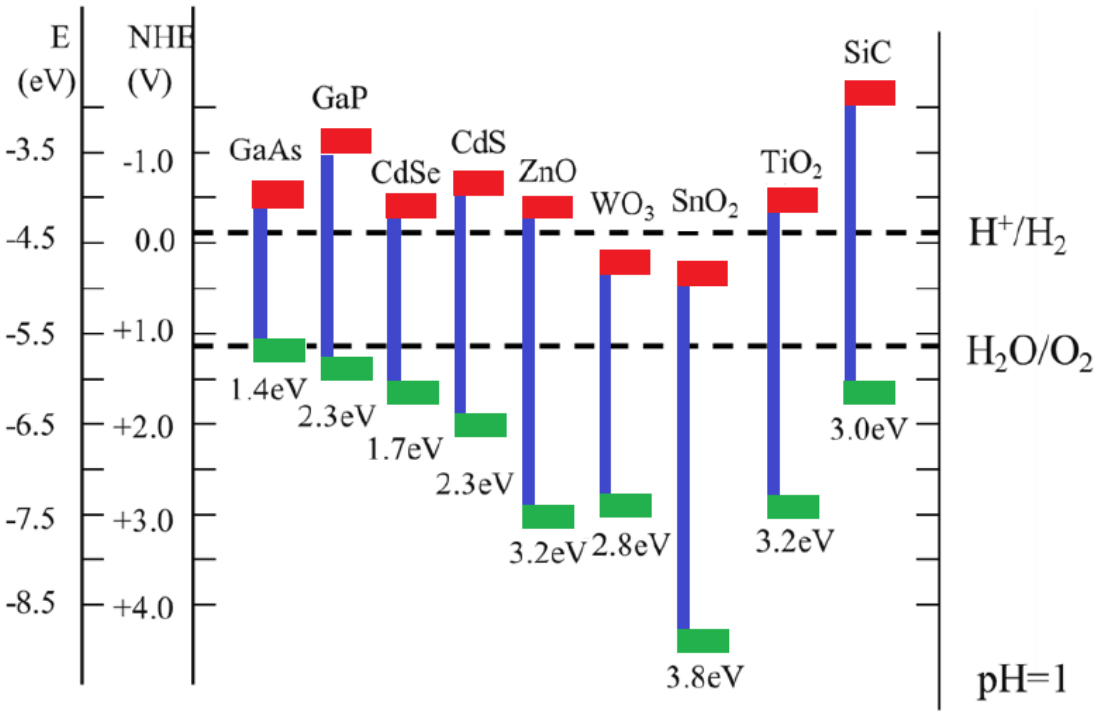

Figure 1.2: Previously reported band positions of selected photocatalysts shown vs. NHE at pH = 1. Image has been adapted from reference 2.

CHAPTER 2

EXPERIMENTAL TECHNIQUES

Hydrothermal Synthesis. In hydrothermal synthesis reagents are mixed in aqueous media and heated under pressure to form a crystalline product. The reactions are carried out in stainless steel autoclaves. In one-step hydrothermal synthesis, the reagent powders are simply added to the autoclave with the aqueous media and heated. The benefits of hydrothermal synthesis include increased solubility of the metal oxide and organic components, relatively quick single crystal growth, and control over several reaction parameters. In hydrothermal synthesis the reaction and crystallization both occur in one vessel in a matter of days and the crystals produced can be of single crystal quality. For example, $V_6O_{10}Cu(C_4H_4N_2)_2 \cdot (H_2O)_{0.22(1)}$ is a dark green block crystal, previously synthesized in the Maggard group that forms in 24 hours at only 115°C.[55] Crystal size, yield of product and byproducts formed can all be controlled by choice of reagents, solvents, pH, temperature, heating time, cooling time, and pressure.

In this research, a one-step hydrothermal synthesis technique was used. Each hybrid was synthesized by adding stoichiometric amounts of the metal oxide or metal organic complex and organic ligands to a 3”×3” FEP Teflon pouch, heat sealing the pouch, placing the pouch inside a polytetrafluoroethylene lined stainless steel autoclave reaction vessel back filled 1/3 (~15 mL) with deionized water, and heated at 125°C for 24 hours in a convection oven.

Solid State and Flux Syntheses. Solid state synthesis and flux synthesis are two methods used for the synthesis of metal oxides. In the ceramic method, metal oxide powders are ground together in a mortar and pestle and heated and reacted at temperatures generally above 500°C. One technique to ensure good contact between particles is pellet pressing. An alternative approach to ensure good contact and lower reaction temperatures is flux synthesis. Flux synthesis works well for metal oxides because the temperature can be lowered from the traditional ceramic method, and the flux can enhance the reactivity of the oxide components through increased solubility of the reactive intermediates. For this research $BaSnO_3$ and La-doped $BaSnO_3$ were synthesized by KCl flux synthesis at 800°C for 6 hours and washed with hot deionized water before being dried in an 80°C oven overnight. $PbTiO_3$ was prepared following a reported procedure that used both solid state and flux synthesis.[56]

Single Crystal X-Ray Crystallographic Structure Determination. Suitable single crystals were dry plated on a microscope slide and submitted to the in house X-ray crystallographer, Paul Boyle. Single crystal X-ray diffraction data sets were collected on a Bruker-Nonius x8 APEX-II CCD diffractometer at ambient temperature (296 K) using graphite-monochromatized Mo Kα radiation ($\lambda = 0.71073$ Å). The frame integrations were performed using the SAINT program. The resulting raw data were scaled and corrected for absorption using a multi-scan averaging of symmetry-equivalent data with the SADABS program. Crystal structures were solved by direct methods through OLEX2 using SHELXS-97. Both structures were refined by the SHELXTL-97 full matrix least squares methods (Sheldrick, 2008).

Electronic Structure Calculations. Electronic structure calculations were performed using the CASTEP package based on plane wave density functional theory and using Perdew-Burke-Ernzerhof functionals in the generalized gradient approximation. The Monkhorst-Pack scheme was used to automatically calculate the k-points within the Brillouin zone.[57,58]

Powder X-ray Diffraction (PXRD). Powder X-ray Diffraction patterns were taken on an INEL XRG 3000 diffractometer using Cu $K\alpha_1$ (λ = 1.54056 Å) radiation from a sealed tube X-ray generator at 35 kV and 30 mA while in transmission mode using a curved position detector (CPS120). The pattern was collected of a 2θ angular range of 0°-106° with a step size of 0.02°. The sample holder was prepared by covering the hole with scotch tape. Then the sample was prepared by scraping a thin layer of dry, ground powder of sample onto the pre-laid scotch tape and covering with another piece of scotch tape. The tape was pressed with a spatula to remove any space or air between the layers. The sample holder was then mounted vertically into a rotating platform. Samples were analyzed from 20 min to 3 hours depending on the sample. Patterns were analyzed in WinPlotr and compared against calculated patterns from the ICSD database using FindIt.

UV-Vis Spectroscopy. UV-Vis diffuse reflectance spectra were taken on a Shimadzu 3600 UV-Vis using a $BaSO_4$ plate. Samples were prepared by taking a small amount of dry, ground sample and pressing it onto a prepared $BaSO_4$ plate. Pressed $BaSO_4$ was used as the reference. Data were measured in reflectance mode and converted to absorbance by the Kubelka-Munk function. The resulting data was first plotted as the remission function

($F(R_\infty)$) = $(1-R_\infty)^2/(2R_\infty)$ based on the Kubelka-Munk theory.[59] Then Tauc plots were plotted from the Kubelka-Munk transformed diffuse reflectance data based on the theory: $(h\upsilon)^{1/2}$ and $(h\upsilon)^2$.[60] The band gap size was estimated using Eg(eV) = λg(nm), where λg was determined by extrapolating the onset of the adsorption edge in the Kubelka-Munk transformed diffuse reflectance spectra.

Infrared Spectroscopy. Infrared spectra were obtained from an IR-Prestige 21 Shimadzu Fourier Transform Infrared (FTIR) Spectrophotometer with a diamond cell sample stage and GladiATR accessory in the range of 200nm-4000nm at a sensitivity of 0.4 for 45 scans per pattern. The sample was prepared by spreading a small amount of dry, ground sample directly on the diamond and clamping down with the pressing arm. Patterns were analyzed using the IRSolutions program with reference spectra coming from the IRSolutions database. Experimental patterns were also analyzed manually using tabulated charts and literature for reference peak positions.

Thermogravimetric Analysis. Thermogravimetric analyses (TGA) were performed on a TA Instruments TGA Q50 under flowing nitrogen gas with various heating programs depending on the sample and test. The sample was prepared by weighing out approximately 10-20 mg onto a clean, dry platinum boat, then equilibrating and tarring at room temperature. The data were plotted as weight percent (wt%) versus temperature (°C). Powder XRD patterns were taken for post-TGA samples (when possible) on the Inel XRG 3000 mentioned earlier in the powder x-ray diffraction section.

Electron Paramagnetic Resonance (EPR). Electron Paramagnetic Resonance measurements were taken on an IBM Instrument Inc. model ER 200D-SRC. The sample was dissolved in deionized water and pipetted into a sealed glass pipet. It was necessary to use water as the solvent because the material would not dissolve readily in any other organic solvent. In order to minimize the effect of water on the response, the path length was reduced by use of the thin portion of a glass pipet. The scan was taken at a sweep width of 2000 and a center field of 3500.

Polycrystalline Film Preparations. Polycrystalline films were prepared by the drop cast method. First, fluorine-doped tin oxide (FTO) glass was cleaned by sonication in deionized water, ethanol, and acetone for 30 min each for 2 cycles. Then a 4 cm^2 square was taped off on the conductive side of the glass by two layers of tape. Samples were ground and suspended in 200 proof ethanol. The suspension was then pipetted and spread onto the FTO in the 4 cm^2 square. The films were then dried at room temperature and the tape removed before annealing. Annealing temperatures varied depending on the material. Additionally, annealing conditions such as annealing under vacuum depended on the experiment and specific details are given in the experimental section of chapter 4 for each relevant material.

Photoelectrochemical Measurements (PEC measurements). Photoelectrochemical measurements were performed in a custom-made Teflon cell (Figure 2.1) using prepared polycrystalline films as the working electrode, platinum as the counter electrode and a standard calomel electrode (SCE) as the reference electrode. Electrolytes used in these

experiments were degassed with Argon gas for 30 minutes prior to use and further degassed throughout the experiments by Argon gas bubbling through the solution during measurement acquisitions. The electrolyte used differed depending on the material uses and the purpose of the PEC measurement. Specific details for this measurement are given in the experimental section of chapter 4 where relevant. Data were recorded by PowerSuite or CH Instruments 620A Electrochemical Analyzer software.

Photocatalytic Oxygen Evolution Experiment. Photocatalytic oxygen gas production measurements were performed using custom-made quartz cells. Approximately 100 mg of sample was added to the quartz cell, along with a stir bar and a 13.5 mmol solution of $AgNO_3$. The solution was degassed with N_2 for 30 min in the dark with stirring. The cell was then transferred to a stir plate in front of a 1000 W Xe lamp and irradiated with UV-Vis light. The quartz cell was fitted with a collection tube which had a bubble of water inserted. The oxygen produced from the photocatalytic oxidation of water in the cell on the photocatalyst sample surfaces was quantified by the measured movement of the bubble in the collection tube and characterized by GC-MS.

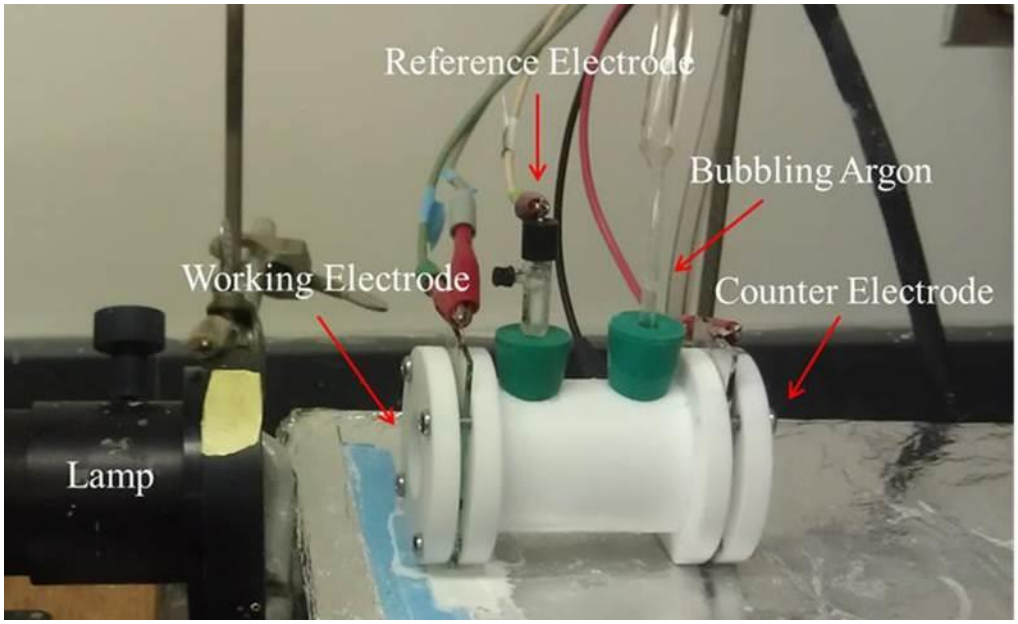

Figure 2.1: Photoelectrochemical cell for all photocurrent measurements.

PART 2

RESULTS

CHAPTER 3

SYNTHESIS AND CHARACTERIZATION OF TWO NEW RU-CONTAINING HYBRIDS

Abstract

Two new heterometallic metal-organic hybrids, $[Ru(C_{10}H_8N_2)_3][NbF_6]_2$ (**I**) and $[Ru(C_{10}H_8N_2)_2(CO)Cl][V_2(C_2O_4)_3O_2(H_2O)]_{0.5} \cdot H_2O$ (**II**) ($C_{10}H_8N_2$ = 2,2'-bipyridine) were synthesized via hydrothermal synthesis and their structures determined by single crystal X-ray diffraction (*P*3c1, Z = 3; *a* = 10.6575(11) Å, *b* = 10.6575(11) Å, *c* = 17.2857(18) Å for **I** and $P2_1/c$, Z = 4; *a* = 8.0168(5) Å, *b* = 11.9369(19) Å, *c* = 27.019(4) Å for **II**). Each hybrid was further characterized by infrared spectroscopy, UV-Vis diffuse reflectance, thermogravimetric analysis, and electronic structure calculations (for **II** only). Structure **I** is comprised of ruthenium tris-bipyridine and niobium fluoride octahedra. Structure **II** is comprised of bi-dentate vanadium-oxalate that is layered along the c axis with distorted ruthenium bis-bipyridine carbonyl complexes. The lowest energy optical transition for structures **I** and **II** occurred at 2.15 eV and 2.54 respectively. Thus incorporating niobium and vanadium causes a blue shift in the absorption spectra for **I** and **II**, relative to the parent ruthenium complexes, $[Ru(C_{10}H_8N_2)_3][Cl_2] \cdot 6H_2O$ and $Ru(C_{10}H_8N_2)_2Cl_2 \cdot 2H_2O$.

Introduction

Heterometallic hybrids have attracted growing research over the past decade for enabling a fine control of the crystal structure at the molecular level.[61-64] For instance, metal

organic vanadates and molybdates form a number of different crystal structures based on the judicious use of organic ligands, causing such materials to be investigated for catalysis, gas absorption, electrical conductivity, and optical absorption properties.[65,66] Specifically, previous work in the Maggard group investigated the interactions between the organic and oxide components of hybrids in order to control structure and target specific physical properties, such as in the M(bipyridine)V_4O_{10} (M=Cu, Ag) systems.[67]

One property of interest for driving photocatalytic reactions, specifically the oxidation and/or reduction of water at the surface of the photocatalytic material, is visible light absorption. As many metal oxide components have large band gap sizes resulting in poor visible light absorption, one approach is the combination of early and late transition metals oxides to vary the band gap size.[30] The conduction band is formed from empty d-orbitals, therefore d^0 cations such as Nb(V) and V(V) will form the conduction band. On the other hand the d^{10} electron configurations of Ag^+ and Cu^+ cations create new lower energy valence bands, reducing the distance between the valance and conduction bands and consequently lowering the band gap size.[68,69] Therefore, copper niobate hybrids were of particular interest in previous work. For example, Haisheng et al. synthesized a series of silver niobate and copper niobate metal organic frameworks through careful selection of organic ligands that could bridge the transition metal centers into 2D and 3D frameworks.[69] The incorporation of both Cu^+ and Ag^+ within the niobate structure shifted the onset of absorption into the visible range.[30] Prior research on ruthenium-based dyes as relatively stable catalysts has led our current research to focus on the synthesis of new heterometallic hybrids containing ruthenium.[33,70,71]

Presented herein are two previously unreported heterometallic metal-organic hybrids containing ruthenium which have formed molecular structures. Both **I** and **II** were characterized by single-crystal X-ray diffraction, UV-Vis diffuse reflectance, thermogravimetric analysis, infrared spectroscopy. Only **II** was further characterized by electronic paramagnetic resonance and electronic structure calculations.

Experimental

Materials: All starting materials used for the syntheses reported were purchased commercially and used as is with no further purification. The starting materials included $[Ru(C_{10}H_8N_2)_3]Cl_2 \bullet 6H_2O$ (Aldrich), Nb_2O_5 (99.99%, Alfa Aesar), $Ru(C_{10}H_8N_2)_2Cl_2 \bullet 2H_2O$ (99%, Strem), NH_4VO_3 (Fisher Scientific), 49% aqueous HF (Fisher Scientific) and oxalic acid (99+%, Aldrich). A quantitative amount of deionized water was also used in the syntheses.

Syntheses: The $[Ru(C_{10}H_8N_2)_3][NbF_6]_2$ (**I**) molecular hybrid was synthesized by hydrothermal method in FEP Teflon pouches placed in a polytetrafluoroethylene lined stainless steel autoclave. The heat-sealed FEP Teflon pouches contained $[Ru(C_{10}H_8N_2)_3][Cl_2] \bullet 6H_2O$ (0.116 g; 0.155 mmol), Nb_2O_5 (0.041 g; 0.155 mmol), 49% aqueous HF (0.062 g; 3.11 mmol), and deionized H_2O (0.279 g; 15.5 mmol) in a FEP Teflon pouch. The polytetrafluoroethylene lined stainless steel autoclave reaction vessel was back filled 1/3 (~15 mL) with deionized water before closing for pressure. The reaction vessel was heated at

125°C for 24 hours in a convection oven. Red-orange rectangular plate and block crystals of **I** formed according to single crystal structure determination of the crystals.

The synthesis of $[Ru(C_{10}H_8N_2)_2(CO)Cl][V_2(C_2O_4)_3O_2(H_2O)]_{0.5} \bullet H_2O$ (**II**) was performed hydrothermally in the same fashion as **I** by adding $Ru(C_{10}H_8N_2)_2Cl_2 \bullet 2H_2O$ (0.038 g; 0.074 mmol), NH_3VO_3 (0.008 g; 0.074 mmol), oxalic acid ($C_2H_2O_4$) (0.067 g; 0.749 mmol), and deionized H_2O (0.134 g; 7.49 mmol) to a FEP Teflon pouch, heat-sealing the pouch, placing the pouch in the polytetrafluoroethylene lined stainless steel autoclave reaction vessel which was back filled 1/3 (~15 mL) with deionized water for pressure before closing. The reaction vessel was heated at 125°C for 24 hours.

Structure Characterization: Single crystal X-ray diffraction data sets for both hybrids were collected on a Bruker-Nonius x8 APEX-II CCD diffractometer at ambient temperature (296 K) using Mo Kα radiation (λ = 0.71073 Å). The frame integrations were performed using the SAINT program. The resulting raw data were scaled and corrected for absorption using a multi-scan averaging of symmetry-equivalent data with the SADABS program. The crystal structures of **I** and **II** were solved by direct methods through OLEX2 using SHELXS-97. Both structures were refined by the SHELXTL-97 full matrix least squares methods (Sheldrick, 2008). Non-hydrogen atomic sites were allowed to refine with anisotropic thermal parameters. The hydrogen atoms were introduced in idealized positions and allowed to ride with the parent carbon or oxygen atoms as relevant. All disordered oxygen/fluorine positions were treated as fluorine positions, but are reported with the appropriate oxygen occupancy according to the chemical formulas below. Details of the

crystal structure refinements are summarized in Table 3.1. Additionally, selected bond lengths and bond angles are reported in Tables 3.S1 and 3.S2 in Appendix A.

IR data were taken using an IR-Prestige 21 Shimadzu Fourier Transform Infrared (FTIR) Spectrophotometer with a diamond cell sample stage and GladiATR accessory in the range of 200nm-4000nm at a sensitivity of 0.4 for 45 scans per pattern. The sample was prepared by spreading a small amount of dry, ground sample directly on the sample stage and clamping down with the pressing arm. Patterns were analyzed using the IRSolutions program with reference spectra coming from the IRSolutions database. Experimental patterns were also analyzed manually using tabulated charts and literature for reference peak positions.

An electronic structure calculation was performed for structure **II** using the CASTEP package based on plane wave density functional theory and using Perdew-Burke-Ernzerhof functionals in the generalized gradient approximation. The Monkhorst-Pack scheme was used to automatically calculate the k-points within the Brillouin zone.[57,58]

Physical Characterization: Thermogravimetric analyses were taken on a TA Instruments TGA Q50. Approximately 50 mg of each hybrid was weighed and loaded onto a platinum pan, where it was equilibrated and tarred at room temperature. The samples were then heated at a rate of 5°/C to 600°C under flowing nitrogen on a TA Instruments TGA Q50.

UV-Vis diffuse reflectance spectra for both hybrid materials were taken on a Shimadzu UV-3600/3100 UV-VIS-NIR spectrophotometer equipped with an integrating sphere, using a pressed $BaSO_4$ plate as the reference. The resulting data was plotted as the

remission function ($F(R_\infty)$) = $(1-R_\infty)^2/(2R_\infty)$ based on the Kubelka-Munk theory.[59] The lowest energy optical transition was estimated using Eg(eV) = λg(nm), where λg was determined by extrapolating the onset of the adsorption peak in the Kubelka-Munk transformed diffuse reflectance spectra.

Results and Discussion

$[Ru(C_{10}H_8N_2)_3][NbF_6]_2$: The $[Ru(C_{10}H_8N_2)_3][NbF_6]_2$ (**I**) crystals are red-orange rectangular plate crystals and the single crystals are orange, thin plates. The overall view of the crystal structure for **I** with the unit cell is shown in Figure 3.1. A layer of $[Ru(C_{10}H_8N_2)_3][NbF_6]_2$ consists of rows of symmetry equivalent ruthenium tris-bipyridine cations and interpenetrating rows of two symmetry non-equivalent niobium hexafluoride anions. Figure 3.2 shows the asymmetric unit along the [001] direction within a layer. There are four symmetry non-equivalent fluorine atoms. Nb1(V) coordinates to three F1 and three F3 fluorine atoms with bond lengths of 1.861(11) Å and 1.913 (15) Å respectively, forming a distorted octahedral anion. Nb2(V) coordinates to three F2 and three F4 fluorine atoms with bond lengths of 1.906(15) Å and 1.865(13) Å, respectively, forming another niobium hexafluoride anion. To counter the two $[NbF6]^{1-}$ anions, the unit cell contains one $Ru(C_{10}H_8N_2)_3^{2+}$ cation. The $Ru(C_{10}H_8N_2)_3^{2+}$ cation is formed by three bi-dentate 2,2'-bipyridine ligands chelating to the Ru^{2+} center to form the distorted $Ru(C_{10}H_8N_2)_3^{2+}$ octahedron. The ruthenium octahedron is distorted as indicated by two symmetry non-equivalent nitrogen atoms with the following bond lengths: Ru-N3, 2.045(15) Å and Ru-N5, 2.084(16) Å. The charge density difference between oxygen and fluorine is negligible, but

when checking overall charge balance and electron count the most chemically sensible assignment is NbF_6. As indicated by the solved crystal structure, **I** is molecular solid.

The thermogravimetric analysis of **I** in Figure 3.4 shows a ~12.95% weight loss up to 425°C, indicating the loss of surface impurities and the 2,2'-bipyridines from the structure. The secondary weight loss is from the fluorine atoms and any remaining organic ligand derivatives. The thermogravimetric analysis is consistent with the structure and formula unit solved from the single crystal data.

The lowest energy optical transition of **I** has been plotted in Figure 3.3. The lowest energy optical transition occurs at 2.15 eV. The small shoulder in the absorption spectra is only 0.005 eV shifted from the than the main absorption peak. Although the main optical transition is blue shifted away from absorbing much of the visible portion of the solar spectrum, $[Ru(C_{10}H_8N_2)_3][NbF_6]_2$ represents a new heterometallic hybrid.

$[Ru(C_{10}H_8N_2)_2(CO)Cl][V_2(C_2O_4)_3O_2(H_2O)]_{0.5} \cdot H_2O$:

The new $[Ru(C_{10}H_8N_2)_2(CO)Cl][V_2(C_2O_4)_3O_2(H_2O)]_{0.5} \cdot H_2O$ (**II**) hybrid structure is shown in Figure 3.5. Along the [001] direction, **II** consists of a bi-dentate vanadium oxalate where the C=C of the bridging oxalate is centered at the corners of the unit cell (not shown in the figure provided). Along the [001] direction is a layer of distorted ruthenium bis-bipyridine chloro-carbonyl molecules. Figure 3.6 shows the asymmetric unit of structure **II** which better elucidates the local coordination, including a structural water molecule on each vanadium center.

The assignment of the two-atom ligand on the ruthenium center is ambiguous owing to several factors. When solving the structure the assignment of the ligand as CN or CO did not yield a better refined solution because the electron-density difference between N and O is small. Further, the bond length, 1.904(4) Å, is consistent with either CN or CO ligands.[71-74] The infrared spectrum (Figure 3.7) also corroborates both possibilities as the stretching frequency for each ligand, when bonded to a ruthenium metal site, falls within overlapping energy ranges (CO = 1950-2100, CN = 2000-2150).[37,75-77] Plus, there are CO stretches arising from the oxalate ligand. In the infrared spectrum, the broad peak just before 3300 cm^{-1} is due to the water in the structure. The sharp peak around 2000 cm^{-1} is attributed to the ambiguous carbonyl or cyano ligand coordinated to the ruthenium. Although there are C=O moieties as part of the oxalate ligand, thus the peak at 2000 cm^{-1} could be the C=O stretching from those moieties, masking any contribution from the diatomic ligand coordinated to the ruthenium site. Again the reference peaks for carbonyl and cyano are shifted into overlapping regions by being bonded to a metal center, preventing a clear indication of which species is coordinated. The rest of the peaks belong to the bending and stretching frequencies of the organic ligands present including 2,2'-bipyridine and the oxalate ligand.

In addition, **II** was further characterized by EPR as shown in Figure 3.8. The number of peaks for Ru(III) is $2(^5/_2) + 1 = 6$ peaks in the range of 3200 to 3600 Gauss. For Ru(I) the literature shows a single EPR signal should be seen around 3400 to 3600 Gauss. The number of peaks that should arise in an EPR spectrum for V(IV) is $2(^7/_2) + 1 = 8$ peaks in the range of 3600 to 4200 Gauss.[70,78-80] Based on the EPR spectrum, V(IV) formed during the reaction. However given the ambiguity of the protons attached to the oxygen atoms of the oxalate

ligand, which may indicate a mixed oxidation state complex. Unfortunately, the EPR spectrum does not directly give the oxidation state of the ruthenium, which means the ligand type cannot be identified. Therefore, another technique is required to determine the oxidation state of ruthenium and ultimately the ligand coordinated to it in structure **II**. One such technique may be linear sweep voltammetry, where Ru^{1+}/Ru^{2+} or Ru^{2+}/Ru^{3+} oxidation and reduction may be seen. The thermogravimetric analysis of **II** is shown in Figure 3.9, and is consistent with formula unit determined by the crystal structure. The first weight loss of 7.4% is due to the loss of surface impurities and the loss of molecular and structural water (calc. 6.7%). As a result of the loss of structural water, the structure collapses by 275°C, as confirmed by an amorphous powder X-ray diffraction pattern of the post-TGA sample.

Diffuse reflectance data of **II**, shown in Figure 3.10, shows the lowest energy optical transition occurs at 2.54 eV and falls at the edge of the visible range of the solar spectrum. This represents a blue shift in the spectrum relative to the parent ruthenium complex, $Ru(C_{10}H_8N_2)_2Cl_2 \bullet 2H_2O$, with its lowest energy optical transition occurring at 1.54 eV. On the other hand the absorption spectrum is red shifted into the visible range compared to the parent V(V) complex NH_4VO_3.

Conclusion

This research investigated the synthesis of new heterometallic hybrids containing ruthenium, resulting in the formation of two new heterometallic hybrids: $[Ru(C_{10}H_8N_2)_3][NbF_6]_2$ (**I**) and $[Ru(C_{10}H_8N_2)_2(CO)Cl][V_2(C_2O_4)_3O_2(H_2O)]_{0.5} \cdot H_2O$ (**II**). Diffuse reflectance data clearly showed that the incorporation of vanadium or niobium

organic complexes blue shifted the lowest energy optical transition relative to parent ruthenium bipyridine complexes. The lowest energy optical transitions for both **I** and **II** are within the edge of the visible range of the solar spectrum. The successful incorporation of these d^0 metals into a hybrid structure containing ruthenium is a promising start for future syntheses in forming Ru(II)/V(V) or Ru(II)/Nb(V) extended solid hybrids.

Table 3.1 Selected crystal data and structure refinement details

	I	**II**
Formula	$[Ru(C_{10}H_8N_2)_3][NbF_6]_2$	$[Ru(C_{10}H_8N_2)_2(CO)Cl]$ $[V_2(C_2O_4)_3O_2(H_2O)_2]_{0.5} \cdot H_2O$
Formula Weight (g/mol)	983.4201	711.90
Crystal color, habit	Plate, Red-orange	Plate, pale yellow
Crystal system	Trigonal	Monoclinic
Space group, Z	P3c1, 3	P121/c1, 4
Temperature, K	296.15 (2)	293 (2)
a, (Å)	10.6575 (11)	8.0168 (5)
b, (Å)	10.6575 (11)	11.9369 (19)
c, (Å)	17.2857 (18)	27.019 (4)
α, (°)	90	90
β, (°)	90	93.032 (3)
γ, (°)	120	90
V, $Å^3$	1700.3 (3)	2599.3 (7)
ρ, (g/cm^3)	2.117	1.850
λ (Å) (MoK_α)	0.71073	0.71073
μ, (mm^{-1})	1.240	1.128
Total Reflections, *R*(int)	34767, 0.0427	53294, 0.0515
Data/Restraints/Parameters	3038/1/71	8896/0/450
R_1, wR_2^a [$I > 2\sigma(I)$]	0.0535/0.1016	0.0398, 0.0914

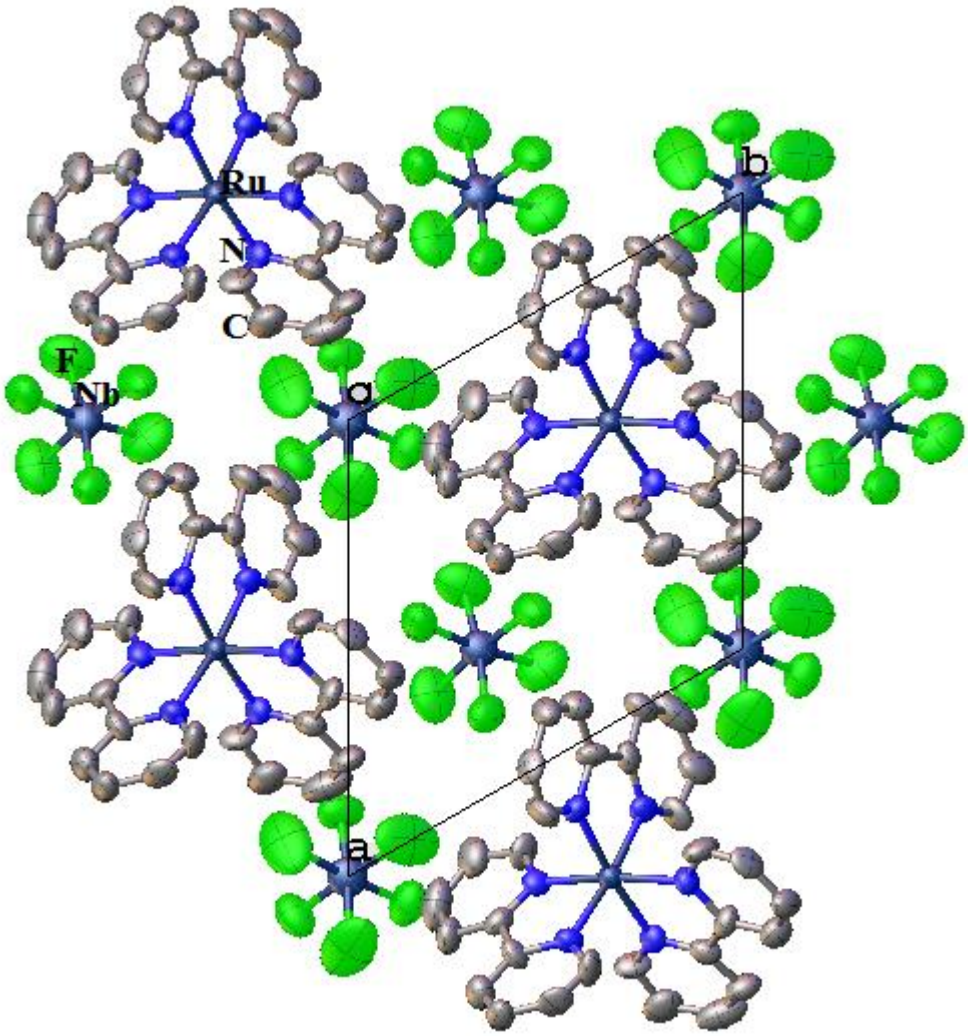

Figure 3.1: Layer of $[Ru(C_{10}H_8N_2)_3][NbF_6]_2$ (**I**) down the [001] direction with the unit cell.

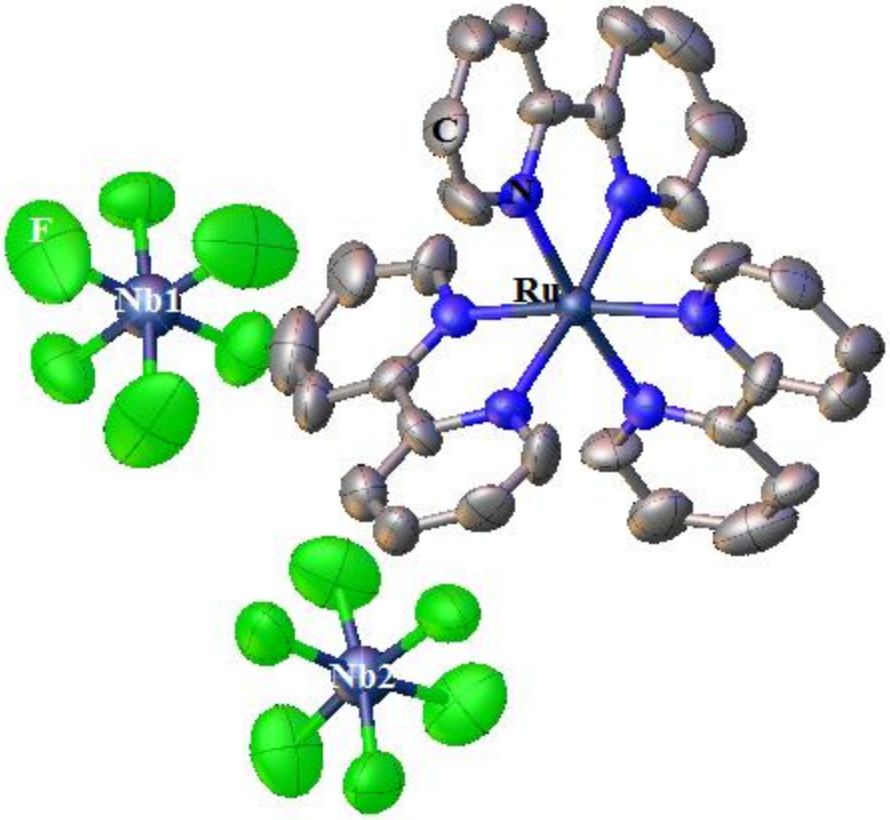

Figure 3.2: Asymmetric unit of $[Ru(C_{10}H_8N_2)_3][NbF_6]_2$ (**I**) down the [001] direction.

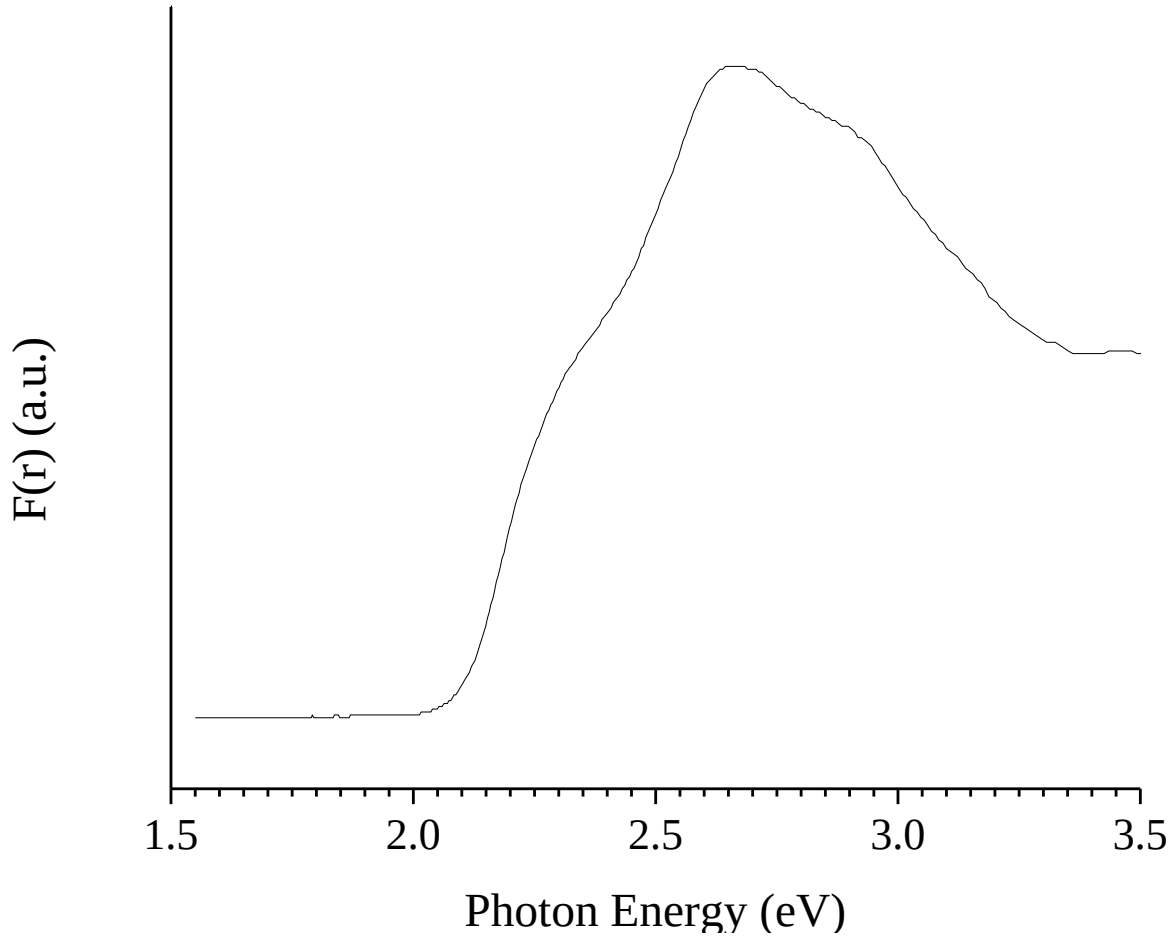

Figure 3.3: Diffuse reflectance spectrum of **I**.

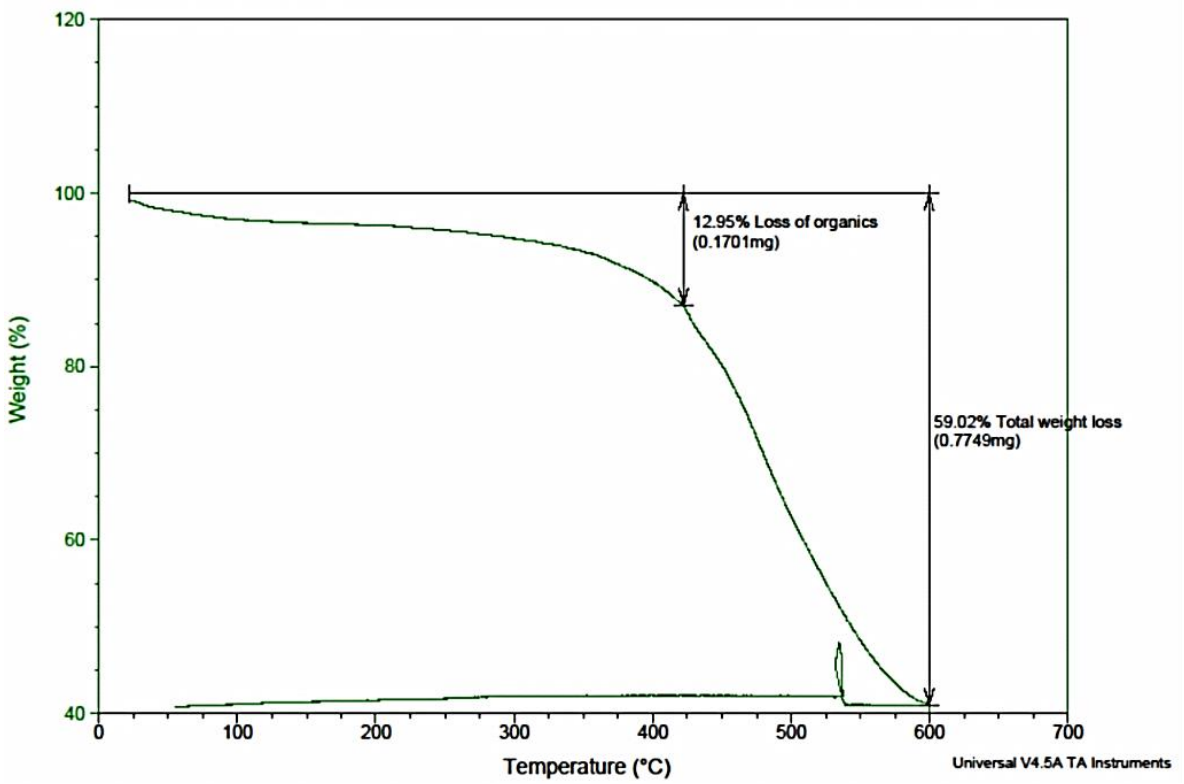

Figure 3.4: Thermogravimetric analysis of **I**.

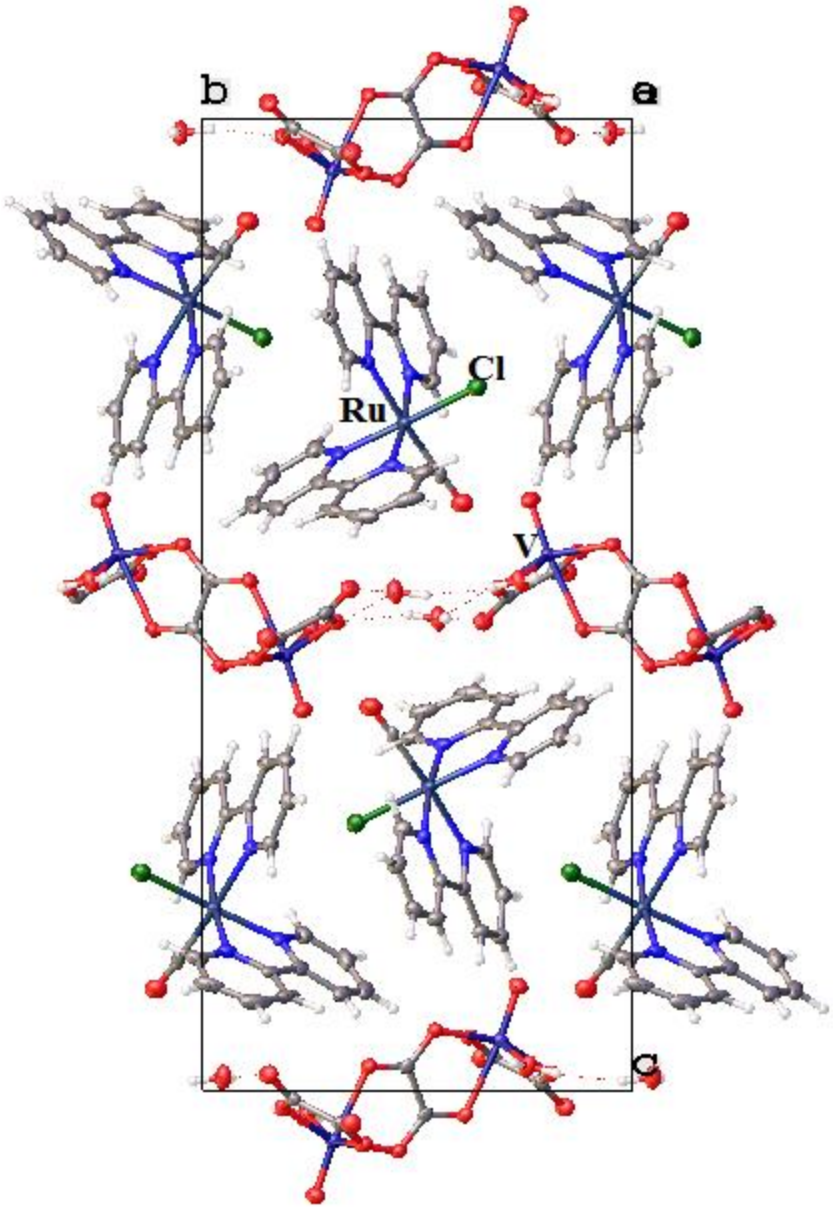

Figure 3.5: Overall view of the unit cell of **II** down the [100] direction.

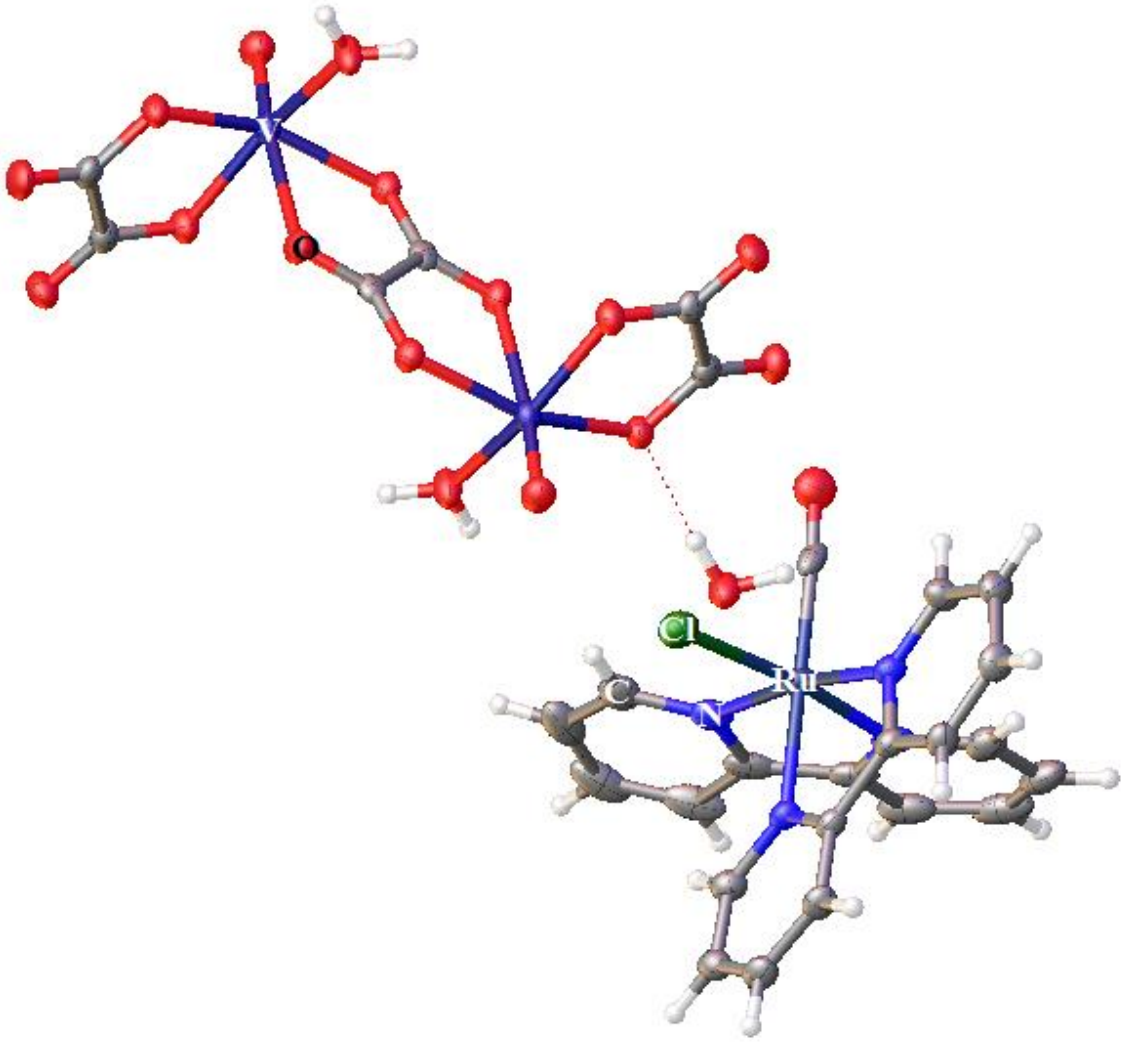

Figure 3.6: Asymmetric unit of **II** along the [111] direction.

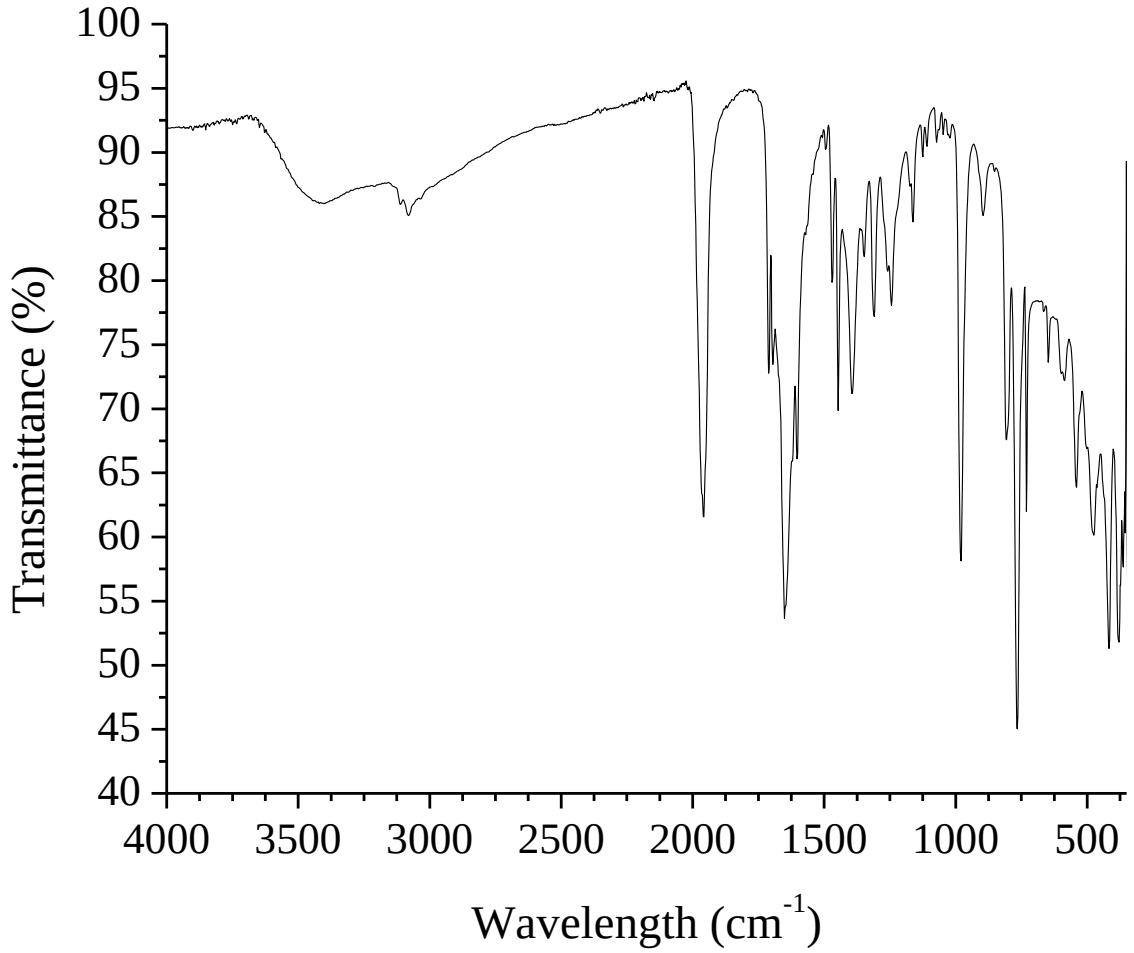

Figure 3.7: Infrared spectrum of **II** from 200 to 4000 nm.

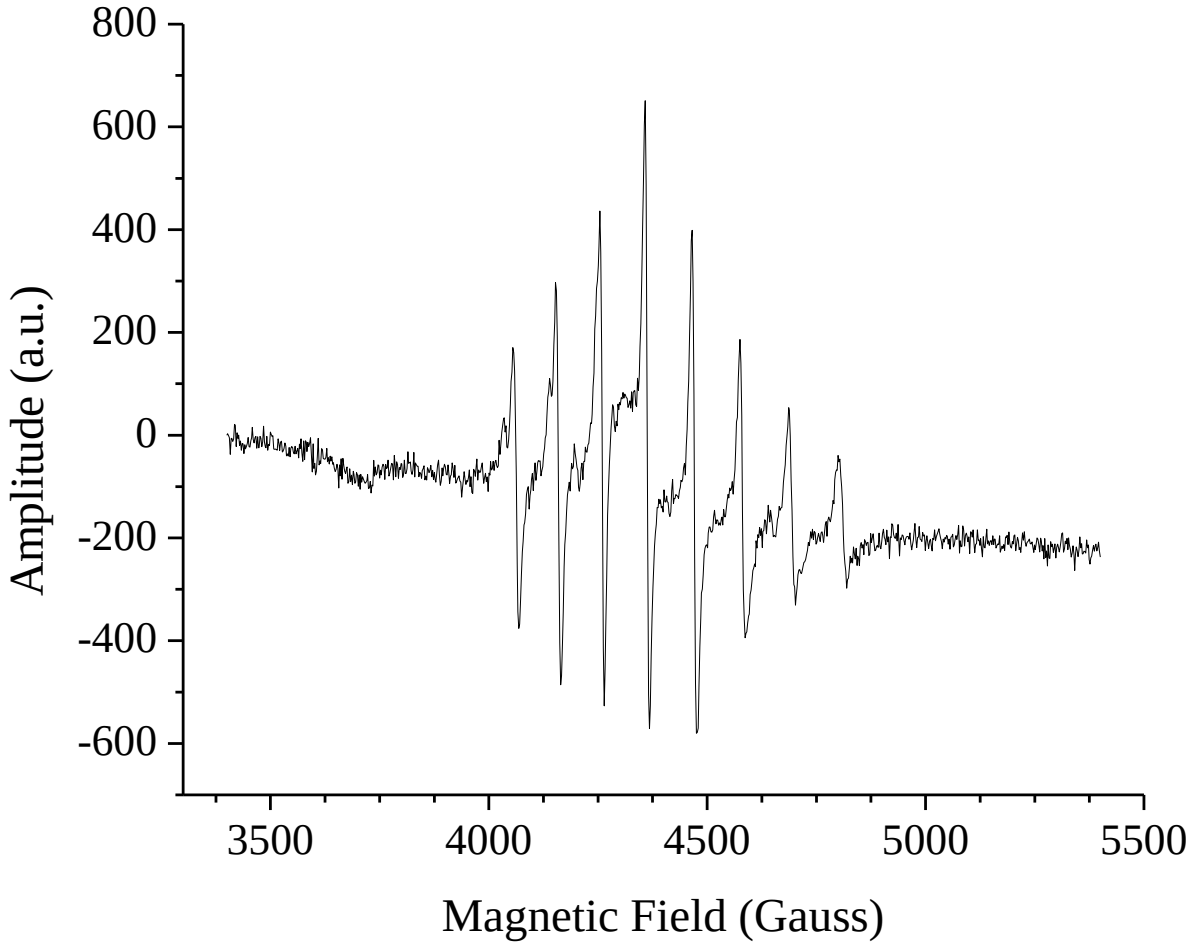

Figure 3.8: Electron paramagnetic resonance spectrum of **II** in water with a sweep width of 2000 and a center field of 3500.

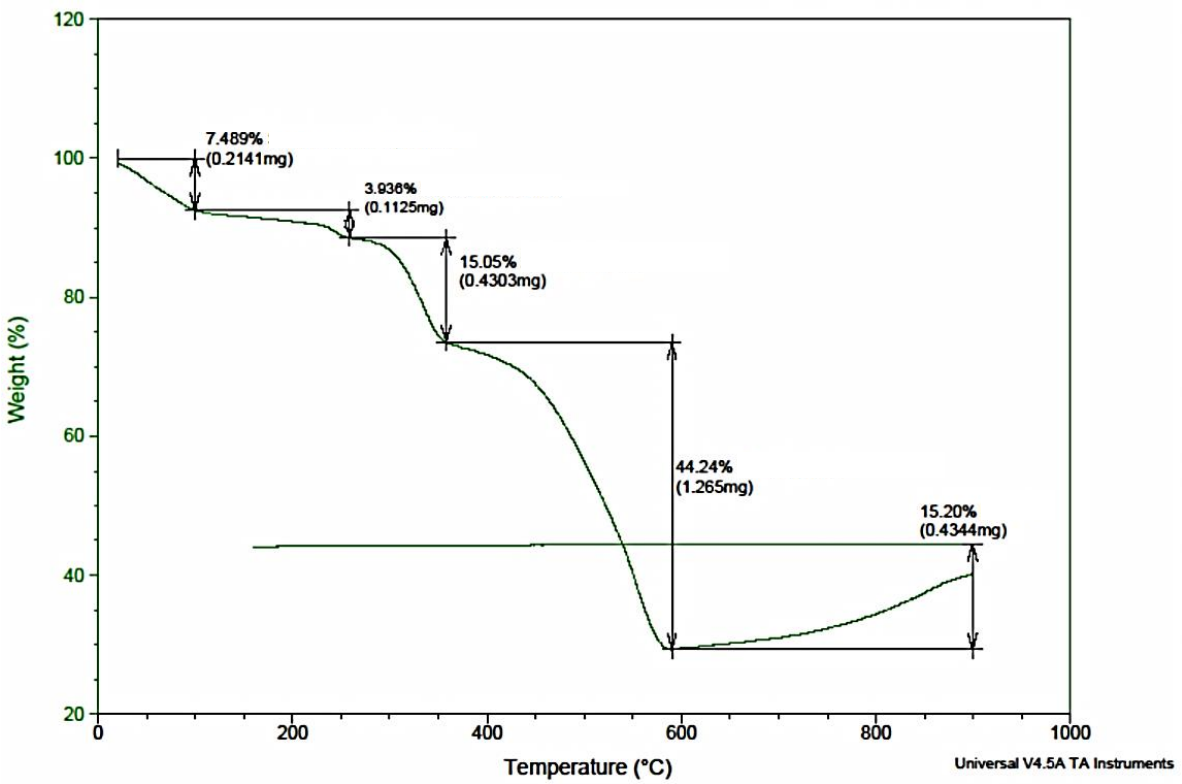

Figure 3.9: Thermogravimetric analysis of **II**.

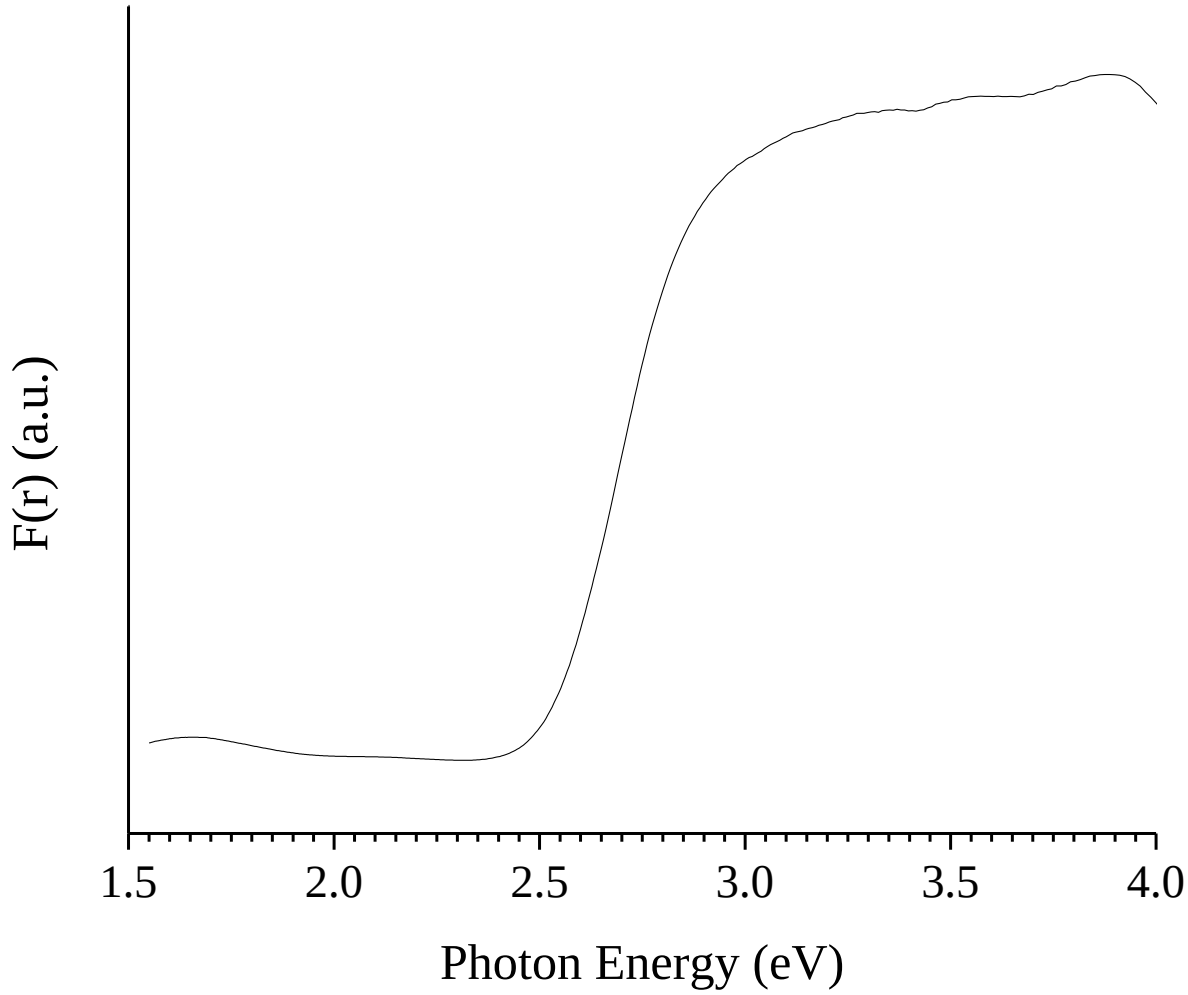

Figure 3.10: Diffuse reflectance spectrum of **II**.

CHAPTER 4

ELECTRONIC, PHOTOCATALYTIC AND PHOTOELECTROCHEMICAL PROPERTIES OF LANTHANUM DOPED ABO_3 PERVOSKITES BARIUM STANNATE AND LEAD TITANATE

Abstract

The ABO_3 perovskites, $BaSnO_3$ and $PbTiO_3$, have been synthesized by the flux method and characterized by powder X-ray diffraction and UV-Vis diffuse reflectance. Electronic structure calculations show measurable band dispersion in their conduction bands suggesting both materials have high charge mobility character. Both are indirect band gap materials, as seen in both the electronic structure calculations as well as in the UV-Vis diffuse reflectance spectra when. The band gaps of $BaSnO_3$ and $PbTiO_3$ were found to be 3.1 eV and 2.5 eV respectively. Doping in La^{3+} cations onto the A site causes a blue shift in the band gap edge of both $BaSnO_3$ and $PbTiO_3$. Photocatalytic and photoelectrochemical measurements show the doping of La^{3+} cations onto the A site of either structure reduces the photocatalytic activity and photoelectrochemical current.

Introduction

Research into photocatalytic O_2 evolution has grown in recent years on the investigation of water splitting photocatalysts to enable clean and renewable energy production and generating questions about the ideal properties that photocatalysts should possess.[10] One of the more prevalent issues with developing the ideal photocatalytic system

is charge separation and transfer being relatively fast compared to the rate of recombination. Many of the best visible-light absorbing photocatalyst suffer from poor charge transfer characteristics, thus preventing the efficient separation and transfer of charges to oxidize and/or reduce water.[7,12,40]

The ABO_3 perovskites are one class of metal oxides whose members have been investigated as H_2 and O_2 evolving photocatalysts, and as thin film scaffolds for dye sensitization.[48,51,81] Research in this area has focused on improving the photoelectrochemical activity of $BaSnO_3$ through approaches such as selecting different B site cations as in Sn^{2+}, Pb^{2+}, and Sb^{3+}, and *n*-type doping with La of the $BaSnO_3$ structure at the A site to increase the number of charge carriers.[49,82-84]It is this latter approach which will be the focus of the research presented herein with initial studies focusing on the improvement of the synthesis of ABO_3 and n-doped ABO_3 species, followed by measurements of the photocatalytic activities of each.

Previous work has been conducted in understanding the electrical, optical and photoelectrochemical properties of $BaSnO_3$ as well as the transport and photoelectrochemical properties of the related $Ba_{1-x}La_xSnO_3$.[45,84-85] For example, oxygen-deficient $BaSnO_3$ is found to have increased conductivity, a smaller band gap size than the parent compound, and the potential for unassisted photocatalytic water splitting due to the conduction band energy.[51] Meanwhile, studies of La-doped $BaSnO_3$ have yielded a small enhancement of the electrical conductivity of parent $BaSnO_3$ owing to the doping of La^{3+} cations into the Ba^{2+} site causing increased conductivity.[53,85-87] The goal of this work is to improve upon both the synthesis and the photocatalytic activity of $BaSnO_3$ and doped $BaSnO_3$, starting with La-doped $BaSnO_3$.

There is one report of the molten flux synthesis of Sr-doped $BaSnO_3$ ($Ba_{1-x}Sr_xSnO_3$).[88] In this study the authors used KOH as the flux and were able to successfully synthesize, in open air, a series of Sr-doped $BaSnO_3$, from pure $BaSnO_3$ to pure $SrSnO_3$. Having confirmed the synthesis of $BaSnO_3$ using this synthesis, the goal was to prepare La-doped $BaSnO_3$ and $PbTiO_3$ by similar flux methods.

Experimental

Materials: All starting reagents were purchased from commercial suppliers including $BaCO_3$ (99.8% Assay, Alfa Aesar), SnO_2 (99.9 % metals basis, Alfa Aesar), La_2O_3 (99.99 % REO, Alfa Aesar) and KOH. All reagents except KOH were dried prior to use with $BaCO_3$ being dried for 24 hours at 750°C in air and both SnO_2 and La_2O_3 being dried for 24 hours at 900°C in air. After drying all reagents were used immediately.

Synthesis: $BaSnO_3$ was synthesized by flux synthesis, using KOH as the alkali flux, from stoichiometric amounts of $BaCO_3$ and SnO_2. The starting reagents were ground together in an agate mortar and pestle. The mixture was added to an alumina crucible containing KOH in a 100:1, 50:1, 40:1, 30:1, 20:1, 15:1, and 10:1 flux:$BaSnO_3$ ratio. The mixture was then heated at 400°C for 6 hours. The product was washed deionized water before being vacuum filtered and dried at 80°C overnight. Lanthanum-doped $BaSnO_3$ was synthesized by flux synthesis using a 40:1 KOH flux ratio from stoichiometric amounts of $BaCO_3$, SnO_2, and La_2O_3, where La_2O_3 was added in a 1, 3, and 5% molar ratio to $BaCO_3$. The dried starting reagents were ground together in an agate mortar and pestle reaction, added to an alumina crucible

containing the KOH flux, and heated at 800°C in air for 6 hours. Non-doped $BaSnO_3$ was also synthesized at 800°C in air for 6 hours.

Structure Characterization: Powder X-ray Diffraction patterns were taken on an INEL XRG 3000 diffractometer using Cu $K\alpha_1$ (λ = 1.54056 Å) radiation from a sealed tube X-ray generator at 35 kV and 30 mA while in transmission mode using a curved position detector (CPS120). The pattern was collected of a 2θ angular range of 0°-106° with a step size of 0.02°. Samples were analyzed from 20 min to 3 hours depending on the sample. Patterns were analyzed in WinPlotr and compared against calculated patterns from the ICSD database using FindIt.

Electronic Structure Calculations: Electronic structure calculations were performed using the CASTEP package based on plane wave density functional theory and using Perdew-Burke-Ernzerhof functionals in the generalized gradient approximation. The Monkhorst-Pack scheme was used to automatically calculate the k-points within the Brillouin zone.[57,58]

Optical Characterization: UV-Vis diffuse reflectance (DRS) spectra were taken on a Shimadzu 3600 UV-Vis using a $BaSO_4$ plate. Samples were prepared by taking a small amount of dry, ground sample and pressing it onto a prepared $BaSO_4$ plate. Pressed $BaSO_4$ was used as the reference. Data were measured in reflectance mode and converted to absorbance by the Kubelka-Munk function. The resulting data were plotted as the remission function ($F(R_\infty)$) = $(1-R_\infty)^2/(2R_\infty)$ based on the Kubelka-Munk theory, and analyzed in the

form of Tauc plots: $(h\upsilon F(R))^{1/2}$ and $(h\upsilon F(R))^{2}$.[59,60] The band gap size was estimated using Eg(eV) = λg(nm), where λg was determined by extrapolating the onset of the adsorption edge in the diffuse reflectance spectra.

Photoelectrochemical and Photocatalysis Testing: Polycrystalline films of non-doped and doped $BaSnO_3$ and $PbTiO_3$ were prepared by the drop-cast method on FTO-conductive glass slides after grinding the product in ethanol with a mortar and pestle. The non-doped and doped $BaSnO_3$ films were annealed at 500°C for 5 hours in air.

Photoelectrochemical (PEC) measurements were conducted in a Teflon cell with a Pt counter electrode and SCE reference electrode using backside irradiation under N_2 gas bubbling and 600W UV-Vis irradiation from a Xe lamp. A 0.5 M Na_2SO_4 electrolyte was used and the pH using 0.05-0.1 M H_2SO_4 or NaOH for $BaSnO_3$. Experiments investigating the non-doped to doped $BaSnO_3$ series used 1M KOH. Electrolytes were degassed with N_2 for 30 minutes prior to testing. Photoelectrochemical data was recorded by a CH Instruments 620A Electrochemical Analyzer software.

Photocatalytic oxygen gas production measurements were performed using custom-made quartz cells. Approximately 100 mg of sample was added to the quartz cell with a stir bar and a 13.5 mmol solution of $AgNO_3$. The solution was degassed with N_2 for 30 min in the dark with stirring. The cell was then transferred to a stir plate in front of a 1000 W Xe lamp and irradiated with UV-Vis light. The quartz cell was fitted with a collection tube which had a bubble of water inserted. The oxygen produced from the photocatalytic

oxidation of water in the cell on the photocatalyst sample surfaces was quantified by the measured movement of the bubble in the collection tube and characterized by GC-MS.

Results and Discussion

Non-doped $BaSnO_3$

$BaSnO_3$ crystallizes in a cubic perovskite structure, ABO_3, of the space group $Pm\bar{3}m$ with Z = 1, a = 4.1148 (3) Å where Ba^{2+} cations sit at the A site and Sn^{4+} cations sit at the B site. The Sn atoms are located on the corner of the unit cell in an octahedral coordination with oxygen. Barium is located within the cavity at the center of the unit cell surrounded by eight tin oxide octahedra (Figure 4.1). $BaSnO_3$ has been successfully synthesized phase pure by flux synthesis in 6 hours at 400°C in air using 100:1, 50:1, 40:1, 30:1, 20:1, and 15:1 KOH flux ratio, shown by the powder X-ray diffraction patterns in Figure 4.2. Note: the slight bump that appears in the 50:1, 30:1, and 15:1 PXRD patterns at 23.9° is from the KOH flux which was not sufficiently washed out in those samples. An indexed powder X-ray diffraction pattern for $BaSnO_3$ can be found in Appendix B (Figure 4.S1).

The optical property of phase pure $BaSnO_3$ was measured by UV-Vis diffuse reflectance. The indirect and direct band gap absorption edges were plotted in Figure 4.3 to confirm that $BaSnO_3$ is an indirect band gap material. The indirect band gap size is 3.1 eV is consistent with the reported UV band gap sizes for $BaSnO_3$ made by solid state ceramic methods, which are ~ 3.10 - 3.18 eV.[89]

The electronic structure of $BaSnO_3$ was calculated using CASTEP. The band structure plot of $BaSnO_3$, shown in Figure 4.4, illustrates the energy of the crystal orbitals of

the valence band and conduction band at given points in k-space. At the bottom of the conduction band at the M point in k-space the orbitals are highly anti-bonding in character. At the Γ point of the bottom of the conduction band the orbitals are non-bonding in character. Then at the R point in k-space for the bottom of the conduction band the orbitals are largely again anti-bonding in character. The large energy band curvature results in a large band dispersion that can lead to high charge mobility for the electrons. For $BaSnO_3$ the top of the valence band is comprised mostly of filled O 2p orbitals. The bottom of the conduction band is comprised mostly of empty Sn 5s orbitals.

Polycrystalline films of phase pure $BaSnO_3$ were measured for photocurrent response at increasing pH values to determine in which pH range the maximum photoresponse could be obtained for this material. For each pH, a new film of the same material was used and the electrolyte solution replaced. Also at each pH a linear scan followed by a cyclic sweep and finally a chronoamperometry scan were measured. The results of the linear and cyclic scans for each pH are overlaid for comparison purposes in Figures 4.5 and 4.6.

The largest photocurrent to dark current was achieved at pH of 3.02. On the other hand, at basic pH, the dark current is extremely low and the response is larger than at neutral pH. This suggests that $BaSnO_3$ has an optimal photocurrent under a basic pH condition. Further support of the conclusion that basic pH is the optimal condition for $BaSnO_3$ is seen in the cyclic voltammograms. Again, the largest current is seen at an acidic pH; however, there is a slight reduction peak that is not reversible. This suggests photocorrosion is occurring on the surface of the $BaSnO_3$ electrode, which is corroborated by the post experiment powder X-ray diffraction pattern reported in Figure 4.S2 (Appendix B). Greater stability is observed for

scans at pH 7.08 and 11.04. Although the photocurrent is not as strong, these films suffered less electrochemical degradation. The final characteristic of the $BaSnO_3$ photoelectrode evaluated in each pH condition was film stability. Film stability translates to both an ability of the semiconducting material to stay adhered to the FTO glass and to remain unchanged throughout electrochemical reactions. Post-PEC PXRD patterns have already shown that the films do not remain unchanged. However, the material does remain securely adhered to the FTO surface. Furthermore, chronoamperometry scans of each film after linear and cyclic scans show photocurrent stability of $BaSnO_3$ at all pH conditions measured (Figure 4.S3 in Appendix B). Ultimately, the initial photoelectrochemical studies of $BaSnO_3$ suggest future studies of La-doped $BaSnO_3$ should be conducted under basic conditions to maximize its photocurrent and stability.

La^{3+} doped $BaSnO_3$

The most pure sample of $BaSnO_3$ by powder X-ray diffraction appears to arise from the 40:1 KOH flux ratio. Thus, the 40:1 KOH flux ratio condition was chosen for all syntheses in which La^{3+} cations were doped into the Ba^{2+} cation site. Non-doped and La-doped $BaSnO_3$ have been successfully synthesized phase pure by flux synthesis according to powder X-ray diffraction patterns, shown in Figure 4.7.

The doping of La^{3+} cations into $BaSnO_3$ was detectable in its lattice parameter shifting, shown in Figure 4.8. As the La^{3+} cation concentration increased the unit cell contracted, which is consistent with the smaller sized La^{3+} (ionic radius = 103 pm) cation replacing the larger sized Ba^{2+} (ionic radius = 149 pm) cation. The smaller cation insertion

into the cavity of the unit cell causes the SnO_6 octahedra framework to contract inward toward the A site.

The optical properties of non-doped and doped $BaSnO_3$ were measured by UV-Vis diffuse reflectance, shown in Figure 4.9. The Kubelka-Munk transformed spectra show a slight red shit in the absorption edge from non-doped to 1% La-doped $BaSnO_3$ that is likely within experimental error. The absorption edges of the 5% and 8% La-doped $BaSnO_3$ samples are more significantly blue shifted from the parent $BaSnO_3$ spectrum.

Non-doped and La-doped $BaSnO_3$ samples were investigated under photoelectrochemical conditions to determine the effect of increasing the charge carrier concentration through *n*-type doping. Figures 4.10 – 4.13 show the linear sweeps in the dark and under 600W UV-Vis irradiation with light chopping, for the $BaSnO_3$ and $Ba_{1-x}La_xSnO_3$ films. The photocurrent density shows a decrease in the photocurrent as La^{3+} cation concentration increased ($BaSnO_3$: ~5 $\mu A/cm^2$, $Ba_{0.99}La_{0.01}SnO_3$: ~2 $\mu A/cm^2$, $Ba_{0.95}La_{0.05}SnO_3$: ~0.25 $\mu A/cm^2$, and $Ba_{0.92}La_{0.08}SnO_3$: ~0.15 $\mu A/cm^2$). The difference in noise between the spectra arises from the electrochemical analyzer package used. The PowerSuite package did not have a detection limit low enough to measure the response from the 5% and 8% films. Thus, those films were measured using the CH Instruments package where the sensitivity of the measurement could be set to detect less than μA responses. This effect of La-doping on the photocatalytic properties of $BaSnO_3$ was also investigated by photocatalytic O_2 evolution experiments. Figure 4.14 plots the O_2 evolution rates of non-doped and La-doped $BaSnO_3$ in the presence of a sacrificial reagent. The sacrificial reagent, $AgNO_3$, was used as an electron acceptor to consume photogenerated electrons in the

conduction band of $BaSnO_3$, because Ag^+ cations are more easily reduced than water. The holes left in the valence band of $BaSnO_3$ are then used to oxidize water to O_2. The gas produced in the suspended particle reactions reported here was confirmed to be O_2 by GC-MS. Doping in La to $BaSnO_3$ was hypothesized to increase the photoelectrochemical response and photocatalytic activity based on the relationship between conductivity and charge carrier concentration (n): $\sigma = ne\mu$. Experimental results suggest other factors are more important to the activity.

Non-doped and La-doped $PbTiO_3$:

Research into ABO_3 perovskites was also conducted for the effect on the photocatalytic activity and photocurrent of high surface area $PbTiO_3$ nanoparticles doped with La^{3+} cations. $PbTiO_3$ nanoparticles have successfully been synthesized following a reported procedure.[56] The article followed includes the solid state synthesis, NaCl flux synthesis, and PbO flux synthesis of $PbTiO_3$. Of the particle sizes reported, the synthesis using a 10:1 NaCl flux:$PbTiO_3$ ratio resulted in the smallest nanoparticles with particles ranging from 75 nm to 180 nm.[56] Thus, all samples tested were synthesized by the reported procedure using 10:1 NaCl as the flux. Powder X-ray diffraction patterns of the phase pure products are shown in Figure 4.15. The insertion of La^{3+} cations into the lattice was indicated by lattice constant refinements showing a slight decrease in the *a* and *c* lattice parameters (Figure 4.16). A decrease in the lattice parameters is expected as the La^{3+} cation is smaller than the Pb^{2+} cation: 103 pm versus 119 pm. The decrease is slight owing to the cations being closer in ionic radii size than La^{3+} cations are to Ba^{2+} cations. The error reported for each

point in Figure 4.16 appears large, but is only ±0.25 Å and results from less accurate peak assignment due to broader peaks in the powder X-ray diffraction pattern that arise from the small nanoparticle sizes of the $PbTiO_3$.

The UV-Vis diffuse reflectance spectra measured did not show any detectable shifting upon doping of La into the structure (Figure 4.17). The band gap sizes were measured to be ~3.0 eV, ranging from 2.96 to 3.04 eV, which is slightly higher than the 2.72 – 2.78 eV band gap sizes reported.[56] However, the non-doped $PbTiO_3$ for this series of reactions and experiments has a band gap of 3.0 eV falling in line with the measured band gaps of the doped samples.

Electronic calculations produced a band structure diagram (Figure 4.18) of $PbTiO_3$ indicating some band dispersion in the conduction band, as expected for the ABO_3 perovskite structure. However as the Pb^{2+} cation has a smaller ionic radius than Ba^{2+} cation (119 pm versus 149 pm), the structure is not ideal and results in less band dispersion. The band structure also indicates $PbTiO_3$ is an indirect band gap material with the top of the valence band at the X point in k space and the bottom of the conduction band at the Z point in k space.

Polycrystalline films of non-doped and doped $PbTiO_3$ were prepared by the drop-cast method on FTO-conductive glass after sonicating the product in ethanol. The polycrystalline films were annealed under vacuum at 400°C for 3 hours. Photoelectrochemical (PEC) measurements were conducted in a Teflon cell with a Pt counter electrode and SCE reference electrode using backside irradiation under N_2 gas bubbling and 600W UV-Vis irradiation from a Xe lamp. A 1M KOH electrolyte solution was used based on previous studies with

$BaSnO_3$, and it was degassed with N_2 for 30 minutes prior to testing. Photoelectrochemical data were recorded by a CH Instruments 620A Electrochemical Analyzer software.

The linear sweep voltammograms of $PbTiO_3$ and $Pb_{1-x}La_xTiO_3$ films are shown in Figures 4.19 to 4.22. The largest photocurrent density is seen for the non-doped film, similar to that found for $BaSnO_3$. However, for the doped $PbTiO_3$ films the photocurrent density increases with increasing La^{3+} cation concentration, though the photocurrent densities of the doped were collectively smaller than that of the non-doped. Furthermore, the films were less stable upon doping as the non-doped film remained adhered to the FTO glass throughout the experiment, whereas the $Pb_{1-x}La_xTiO_3$ films began to fall off during the experiments with the 5% and 8% films completely dislodging from the glass. Nonetheless, both linear sweep voltammograms as well as chronoamperometry scans were able to be measured. The chronoamperometry scans are reported in Figure 4.S4 in Appendix B. Despite the lack of physical adherence of the $Pb_{0.95}La_{0.05}TiO_3$ and $Pb_{0.92}La_{0.08}TiO_3$ films, these films were the most stable electrochemically as seen by the lack of current density degradation as seen in the chronoamperometry scans.

Photocatalytic O_2 production measurements of the $PbTiO_3$ and $Pb_{1-x}La_xTiO_3$ suspended particles are consistent with the photoelectrochemical data. Figure 4.23 illustrates the production of O_2 versus time. As with $BaSnO_3$, the non-doped sample has a much greater activity than the doped analogs. One possible explanation for the reduction in activity is the loss of efficient charge transfer pathways from the incorporation of La^{3+} cation defects and the Ba^{2+} or Pb^{2+} cation vacancies generated from the necessary removal of three Ba^{2+} or Pb^{2+} cations for the insertion of every two La^{3+} cations.

Conclusions

$BaSnO_3$ was *n*-type doped with La^{3+} cations to increase the charge carrier concentration in order to increase the conductivity and ultimately the photoresponse. However, photoelectrochemical and photocatalytic O_2 evolution measurements showed a decrease in the photoresponse and photocatalytic activity upon *n*-type doping with La^{3+} cations. Photoelectrochemical and photocatalytic O_2 evolution measurements of $PbTiO_3$ also showed a decrease in photoresponse and photocatalytic activity when comparing the non-doped $PbTiO_3$ with the La-doped $PbTiO_3$. However, the expectation of an increase in photocatalytic activity due to increased charge carrier concentration increasing the conductivity has initial support from the experimental data as there was a slight increase in the photoresponse and photocatalytic activity with increasing dopant concentration relative to the series of doped samples only. Ultimately, *n*-type doping of two ABO_3 perovskites has suggested that this approach may not successfully enhance the photoresponse or photocatalytic properties.

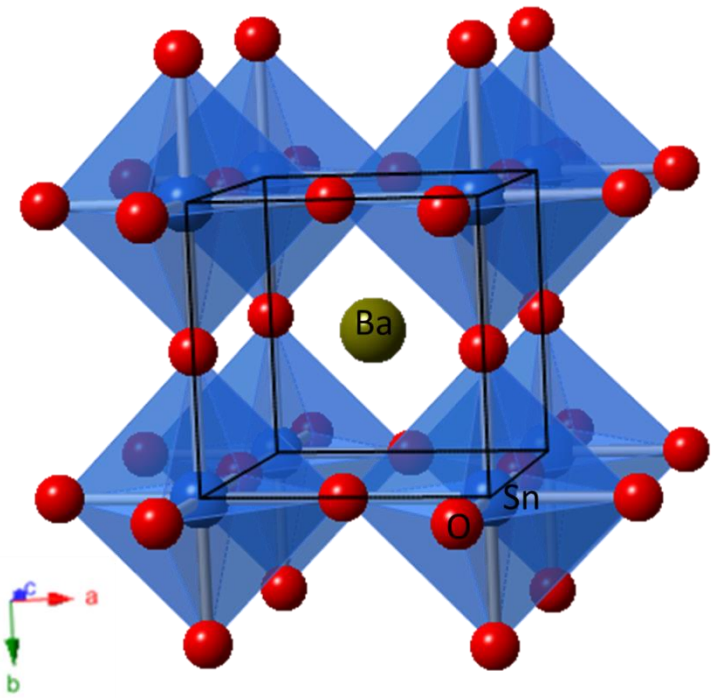

Figure 4.1: Crystal structure of $BaSnO_3$ with the unit cell outlined in black.

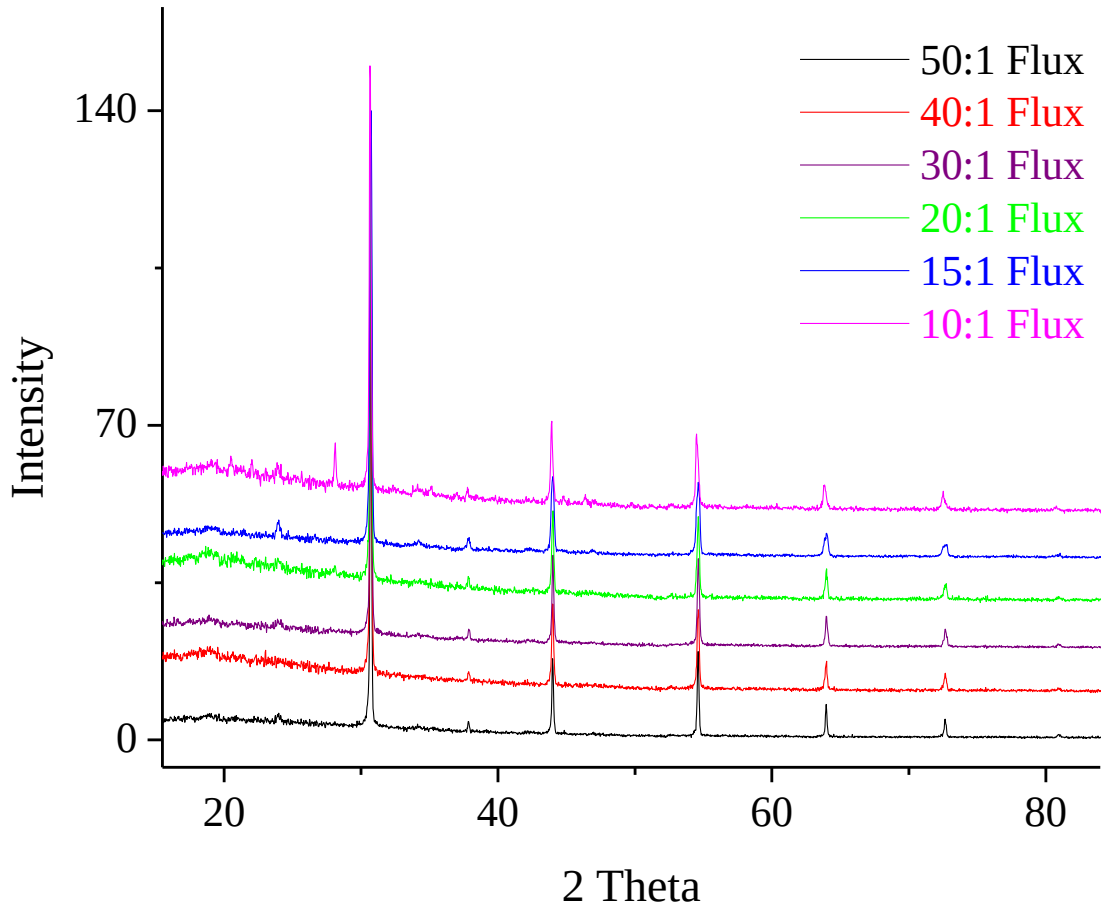

Figure 4.2: Powder X-ray diffraction patterns of $BaSnO_3$ synthesized by KOH molten flux synthesis in flux ratios of 50:1, 40:1, 30:1, 20:1, 15:1, and 10:1.

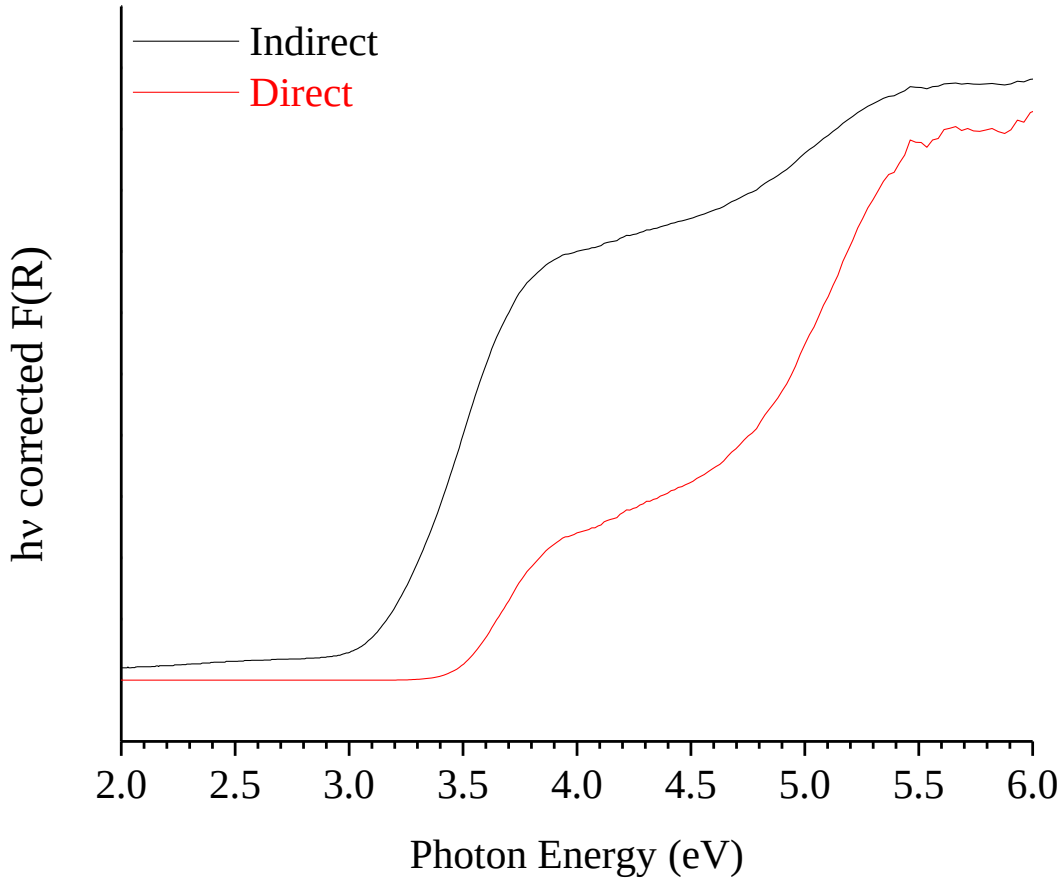

Figure 4.3: Tauc plots of diffuse reflectance spectra of $BaSnO_3$.

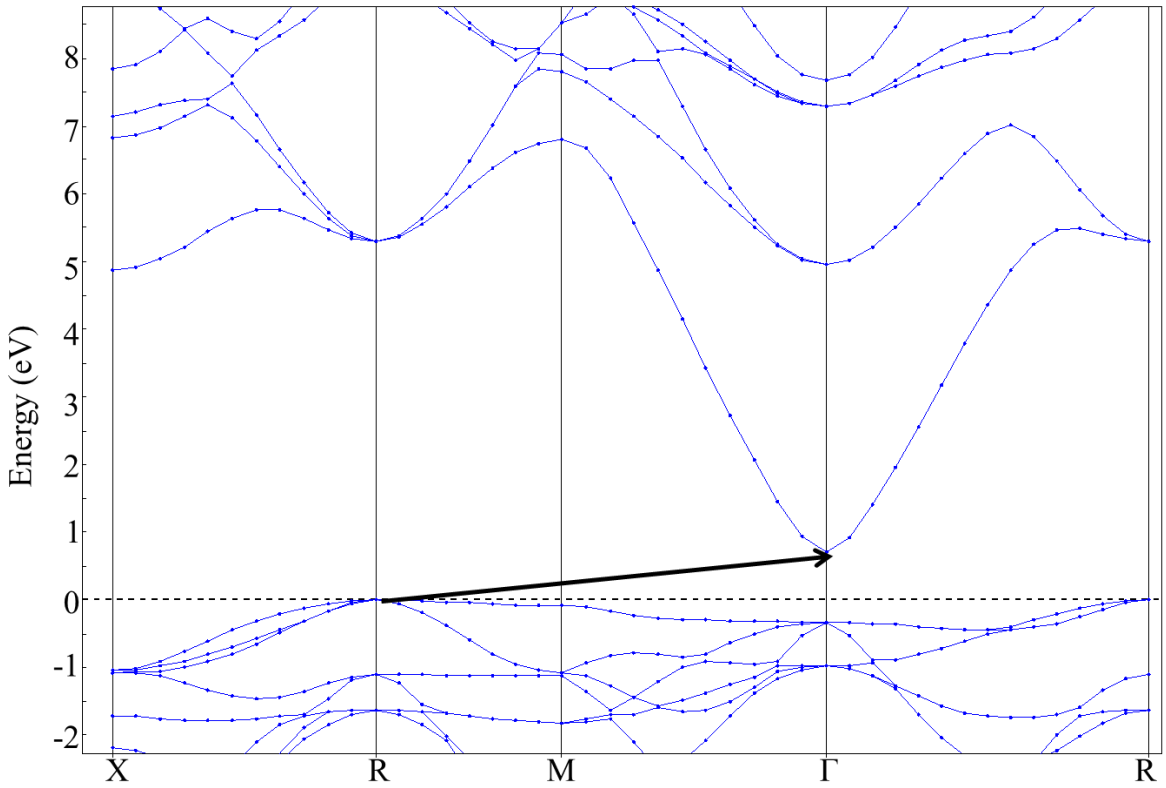

Figure 4.4: Band structure of $BaSnO_3$. The top of the valence band is at the R point and the bottom of the conduction band is at the Γ point resulting in an indirect band gap.

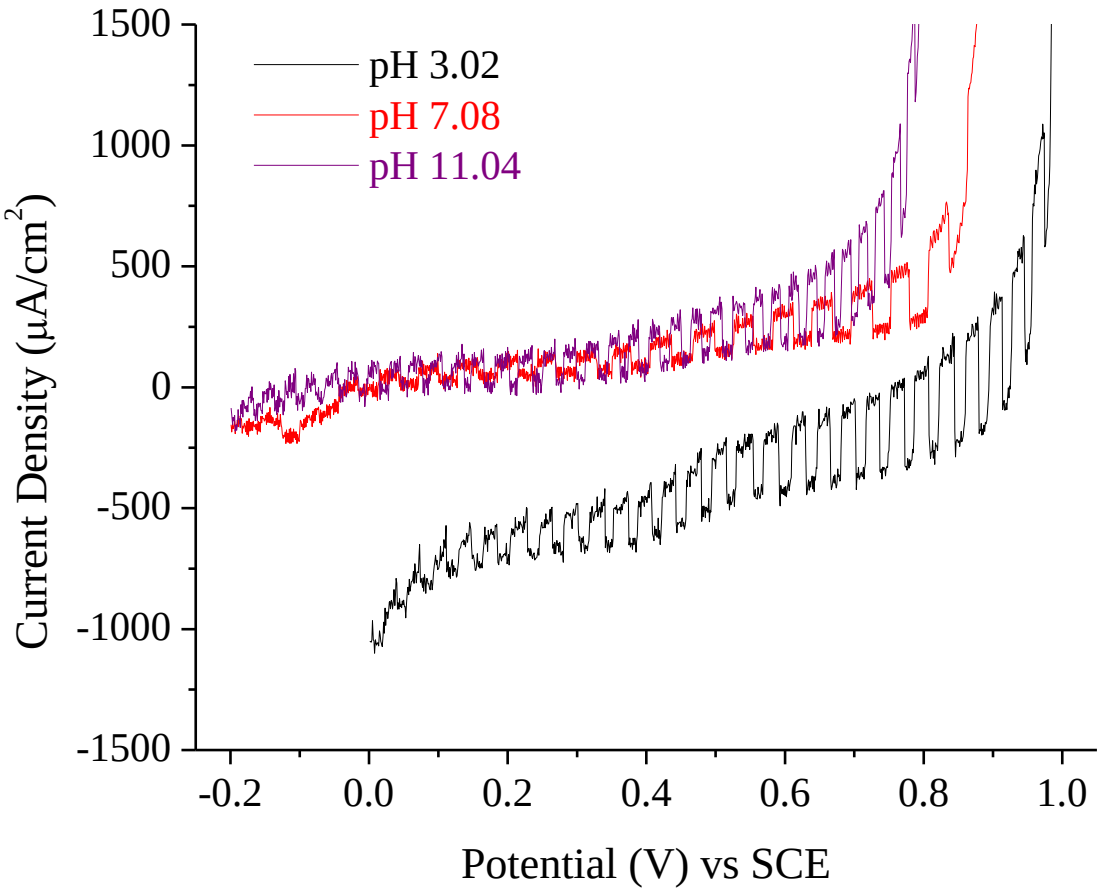

Figure 4.5: Linear voltammograms of $BaSnO_3$ films in 0.5 M Na_2SO_4 at pH 3.02, 7.08, and 11.04. Scan rate of 10mV/s.

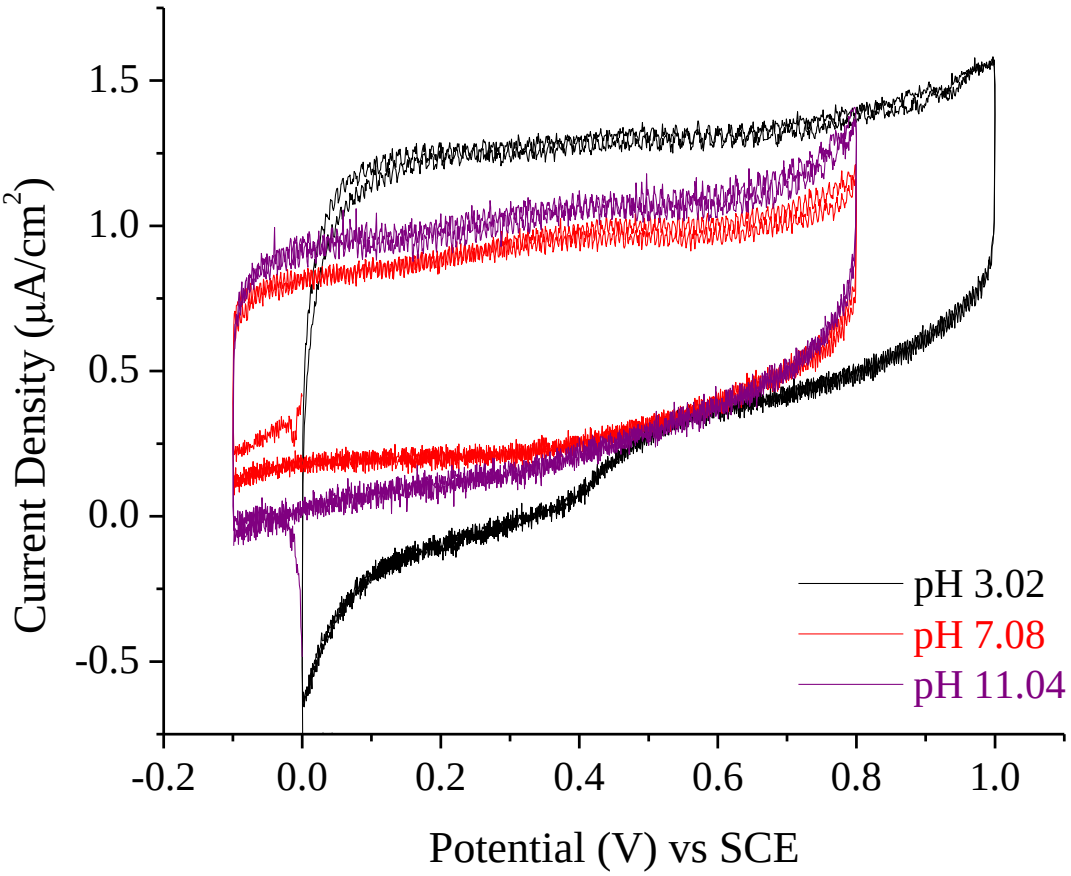

Figure 4.6: Cyclic voltammograms of $BaSnO_3$ films in 0.5 M Na_2SO_4 at pH 3.02, 7.08, and 11.04. Scan rate of 10mV/s for 5 cycles.

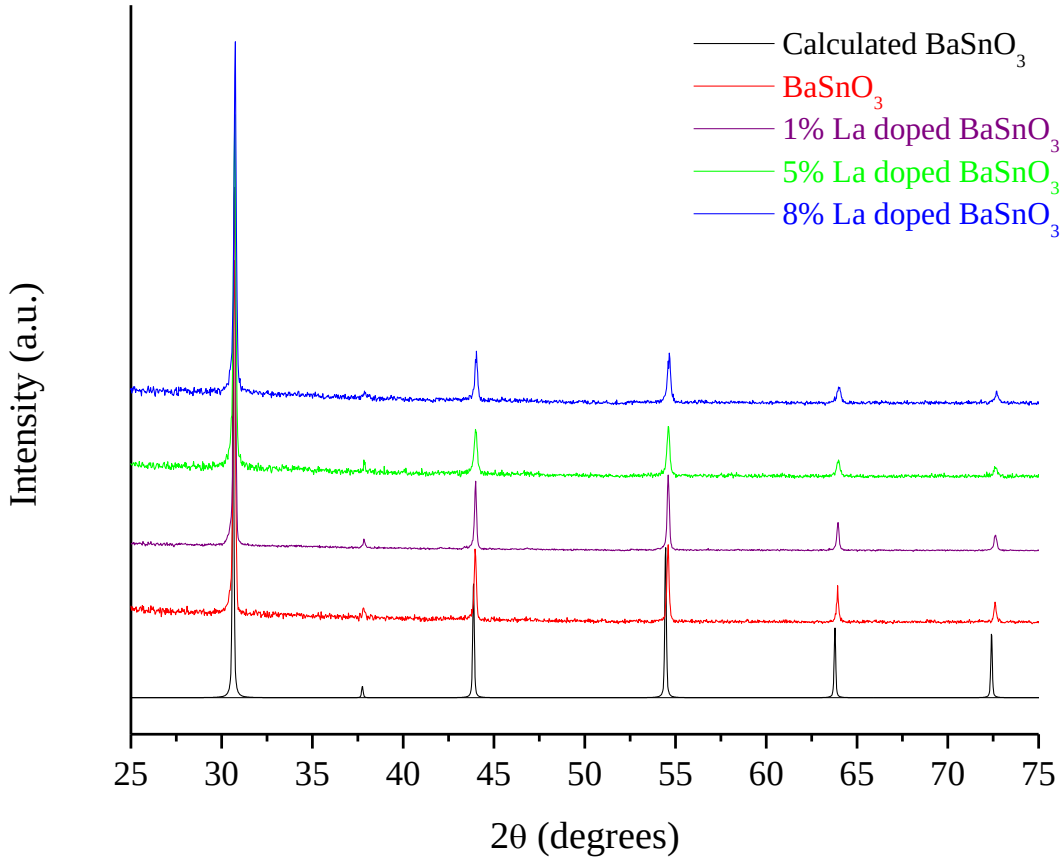

Figure 4.7: Powder X-ray diffraction patterns of La-doped $BaSnO_3$ synthesized by KOH molten flux synthesis in a 40:1 flux ratio at 800°C.

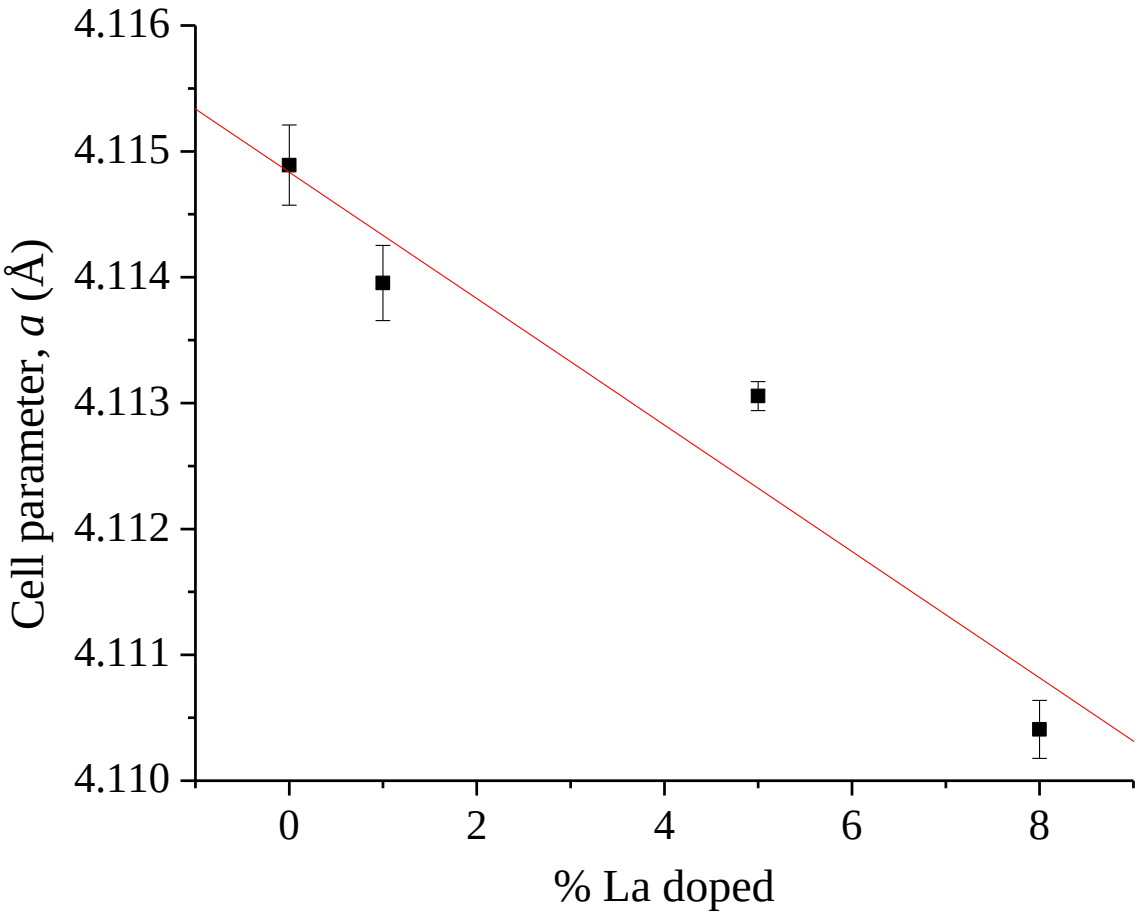

Figure 4.8: The change in the *a* lattice parameter as a function of La dopant concentration of non-doped and doped $BaSnO_3$ from the powder X-ray diffraction patterns.

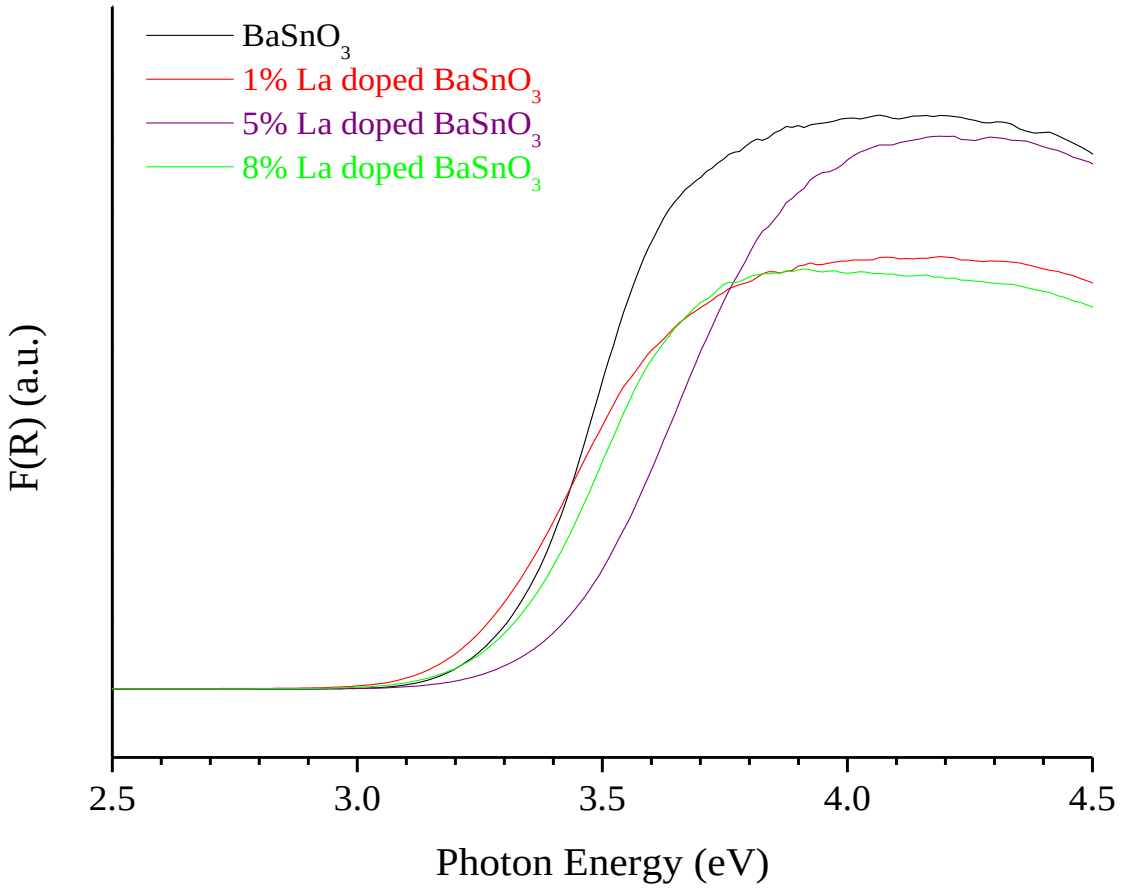

Figure 4.9: Diffuse reflectance spectra of $BaSnO_3$ and La-doped $BaSnO_3$.

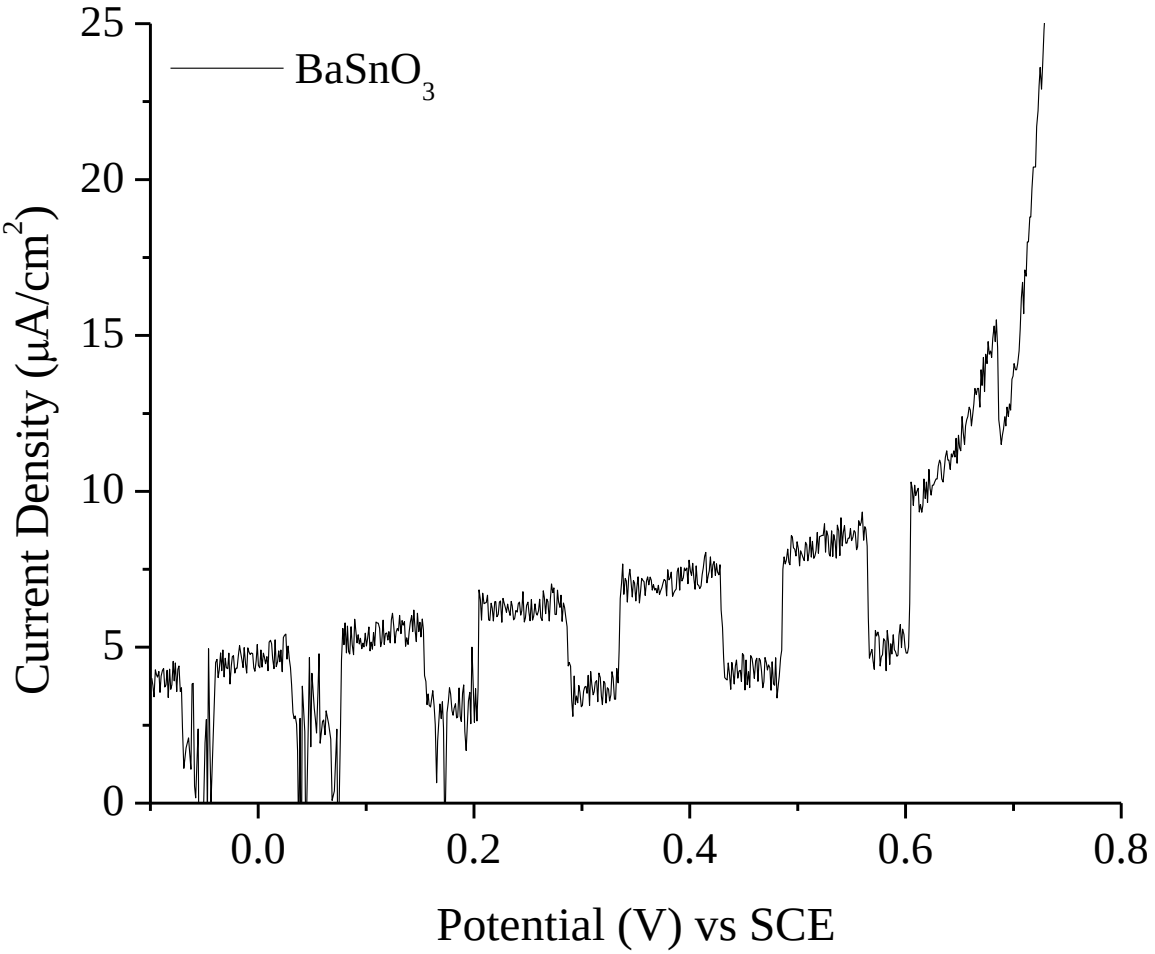

Figure 4.10: Linear sweep in 1M KOH under light chopping at 80 bpm of 600W UV-Vis irradiation of a $BaSnO_3$ film prepared by the drop-cast method and annealed at 500°C.

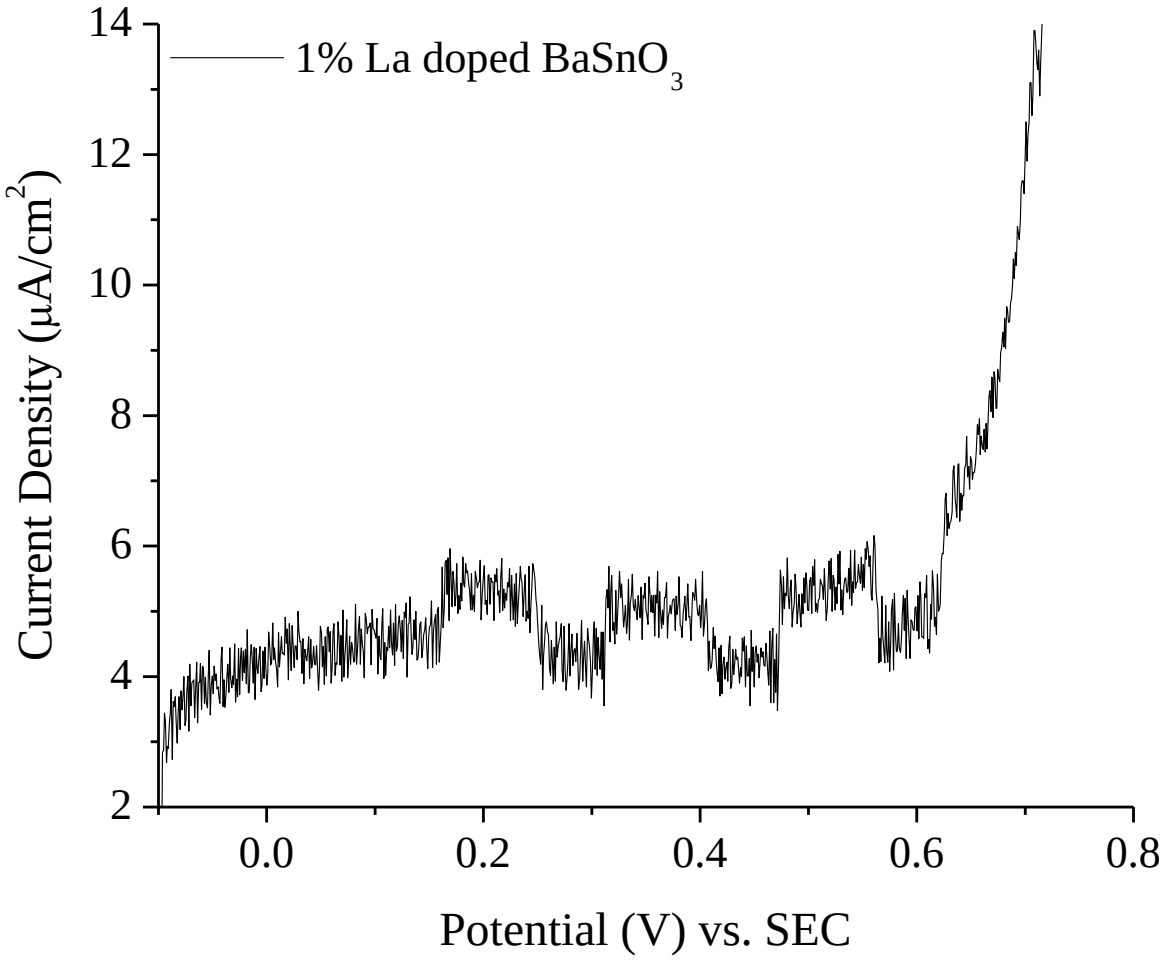

Figure 4.11: Linear sweep in 1M KOH under light chopping at 80 bpm of 600W UV-Vis irradiation of a $Ba_{0.99}La_{0.01}SnO_3$ film prepared by the drop-cast method and annealed at 500°C.

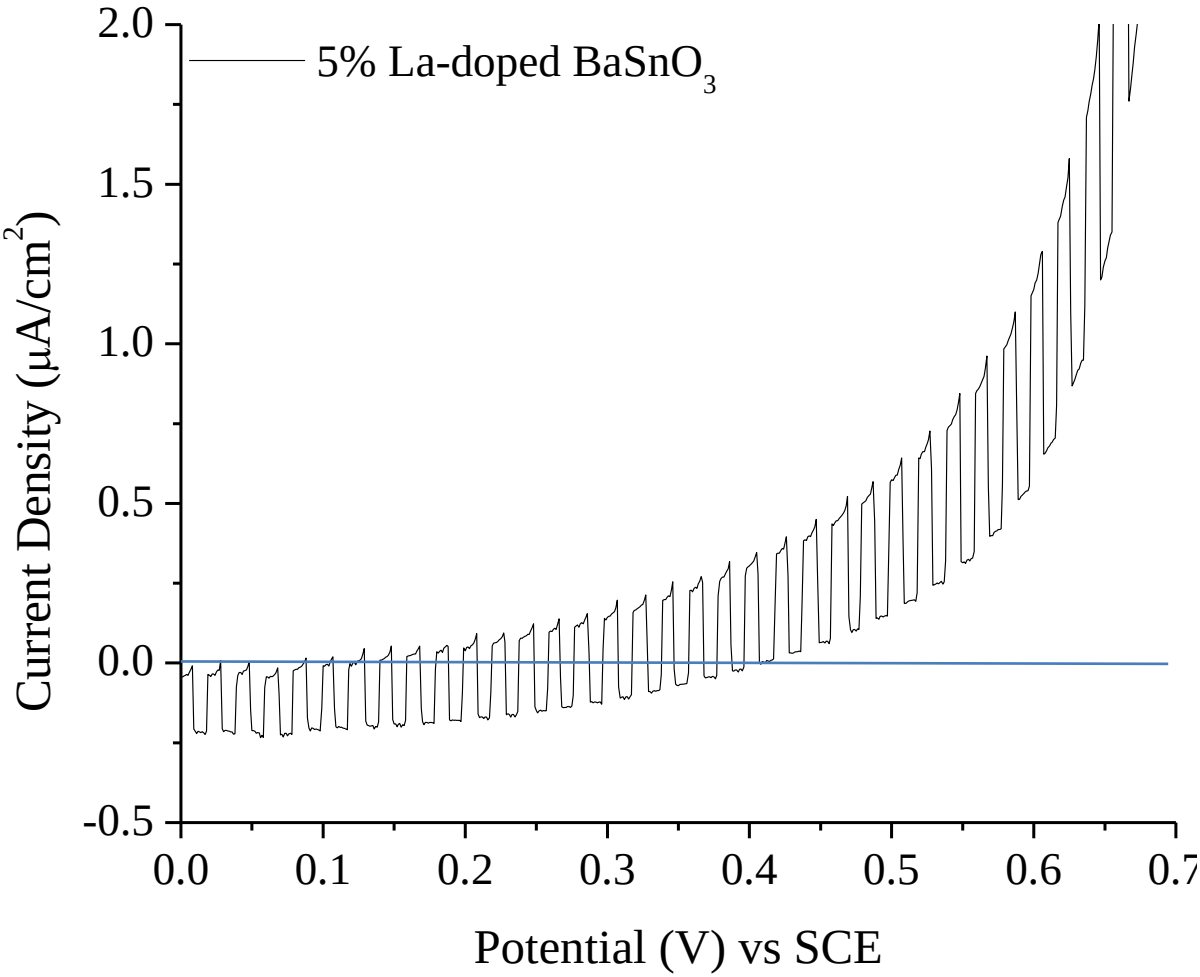

Figure 4.12: Linear sweep in 1M KOH under light chopping at 60 bpm of 600W UV-Vis irradiation of a $Ba_{0.95}La_{0.05}SnO_3$ film prepared by the drop cast method and annealed at 500°C.

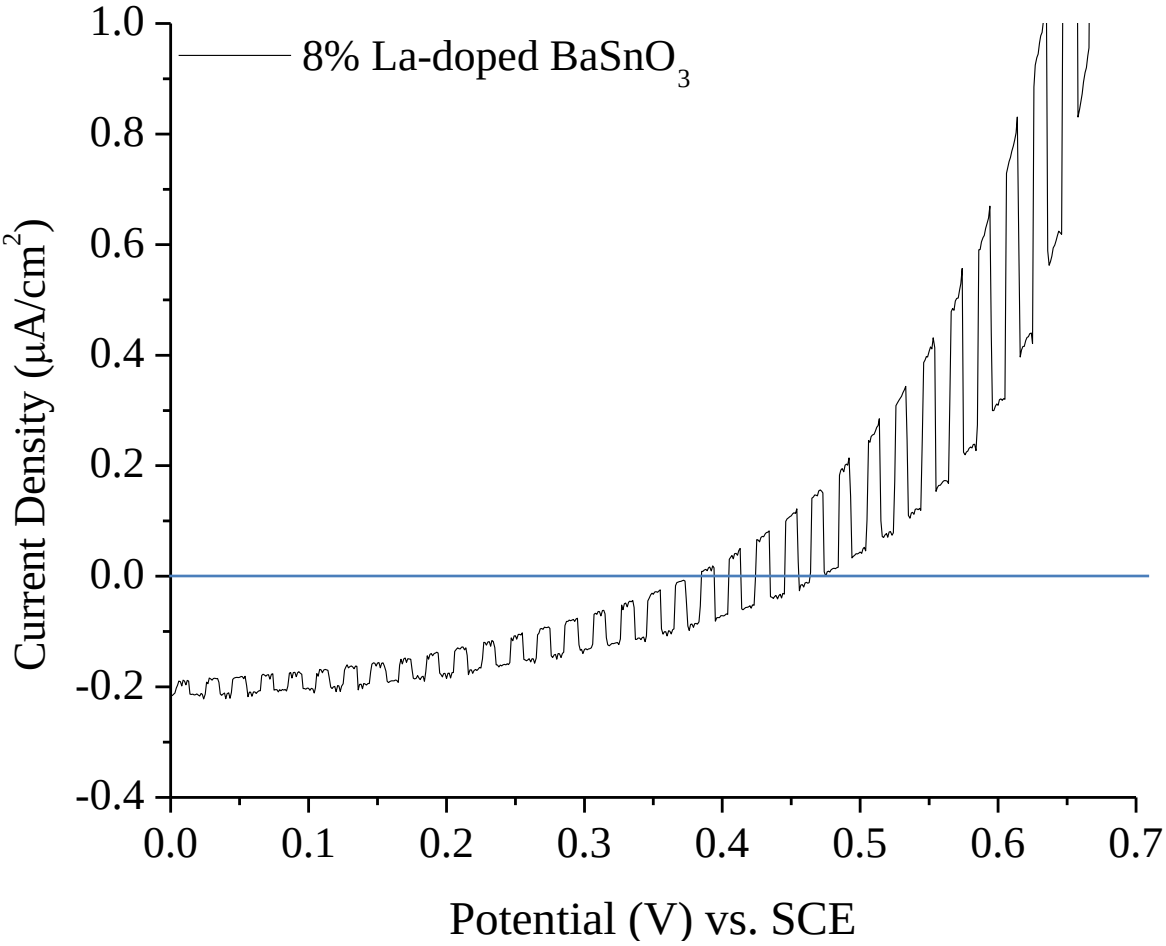

Figure 4.13: Linear sweep in 1M KOH under light chopping at 60 bpm of 600W UV-Vis irradiation of a $Ba_{0.92}La_{0.08}SnO_3$ film prepared by the drop cast method and annealed at 500°C.

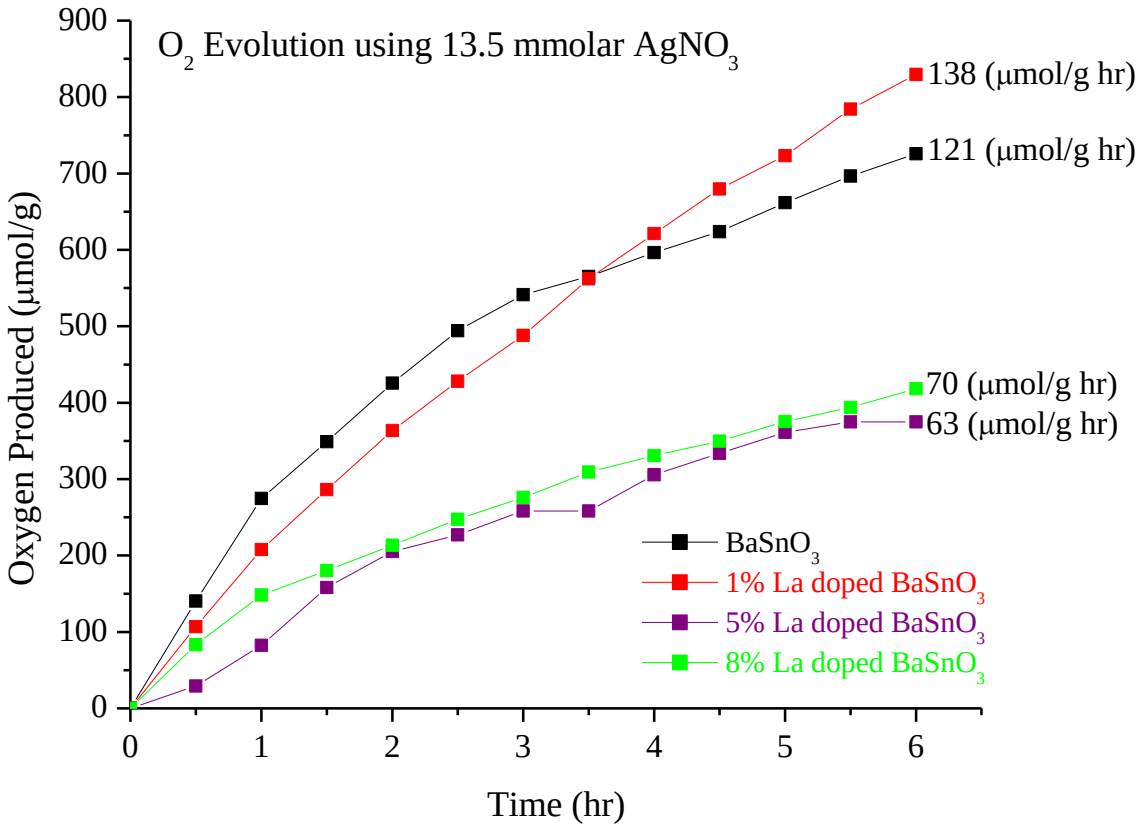

Figure 4.14: Oxygen evolution with average rates of doped and non-doped $BaSnO_3$ in a 13.5 mmolar $AgNO_3$ solution under UV-Vis light with stirring.

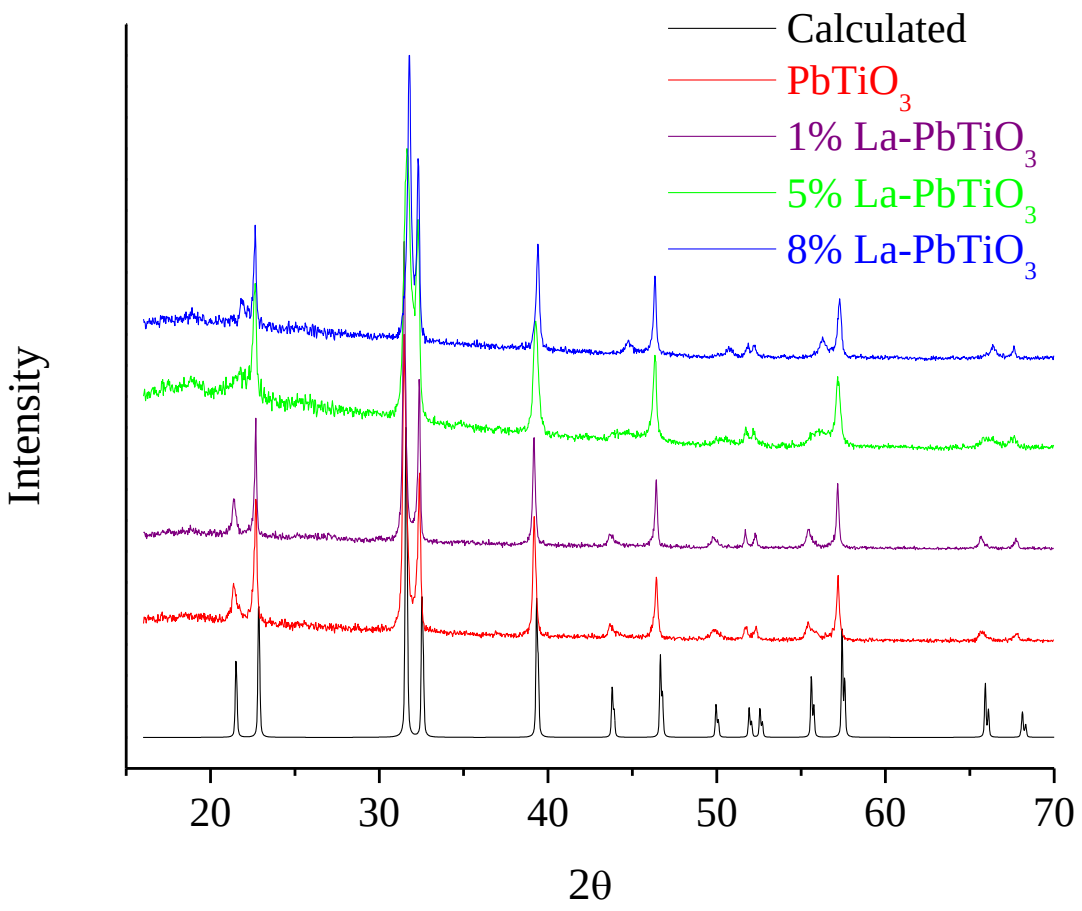

Figure 4.15: Powder X-ray diffraction patterns for non-doped and doped $PbTiO_3$ synthesized by 10:1 NaCl flux at 1000°C in air for 1 hr.

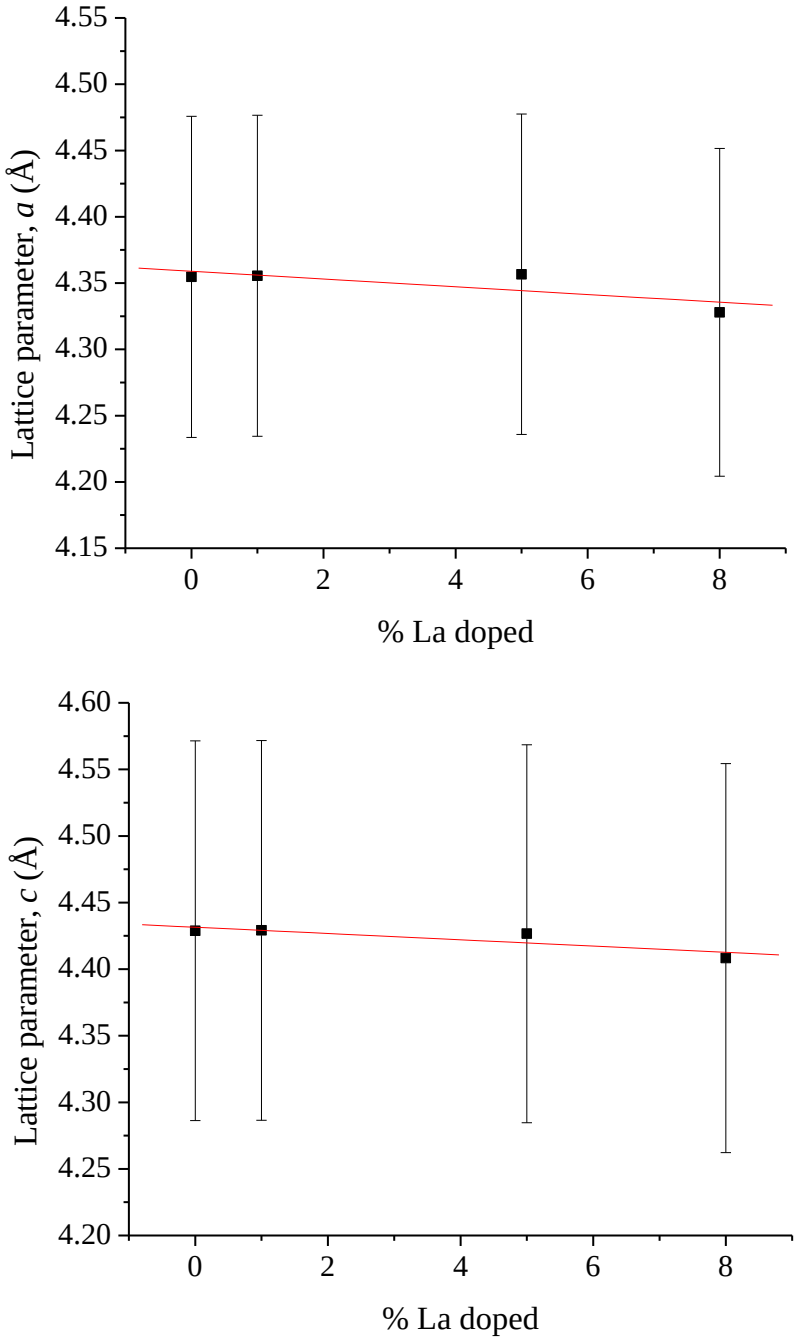

Figure 4.16: The change in the *a* (top) and *c* (bottom) lattice parameters as a function of La dopant concentration of non-doped and doped $PbTiO_3$ from the powder X-ray diffraction patterns.

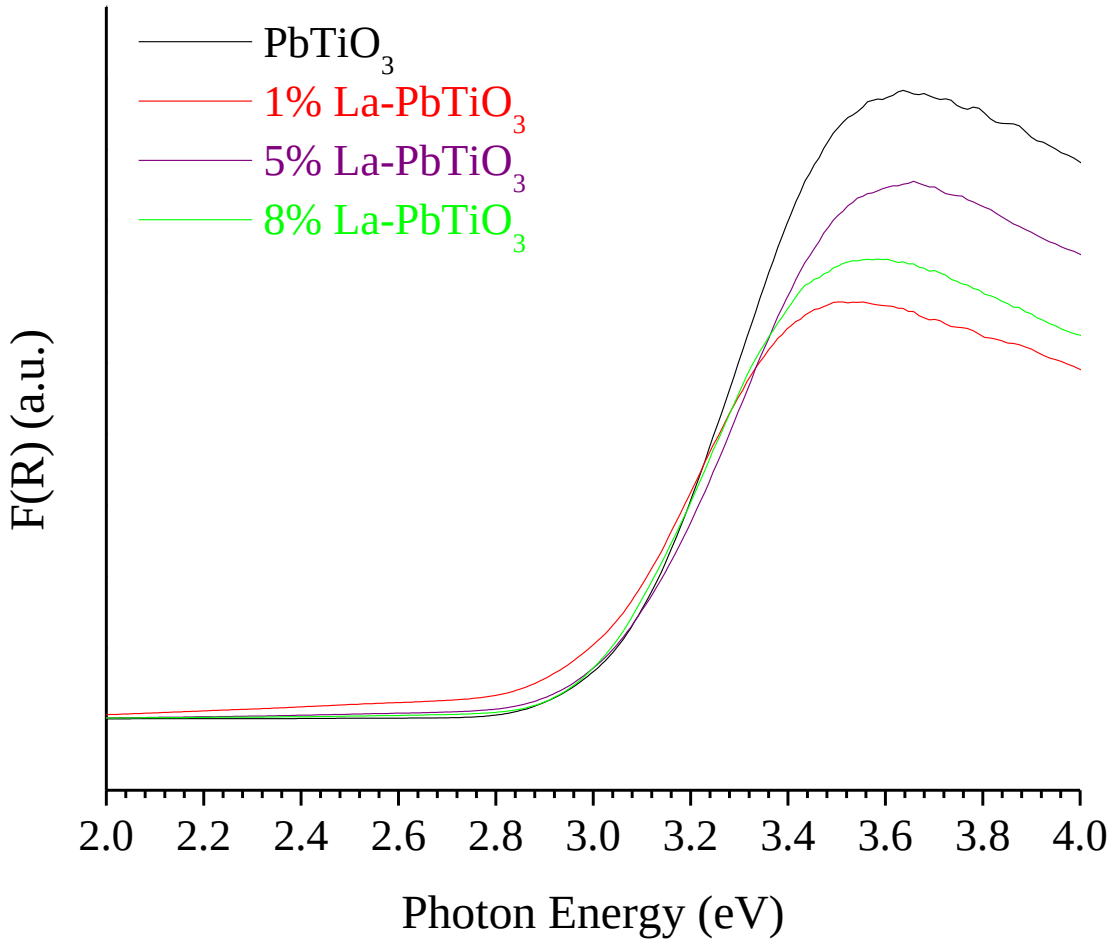

Figure 4.17: Diffuse reflectance spectra of $PbTiO_3$ and La-doped $PbTiO_3$.

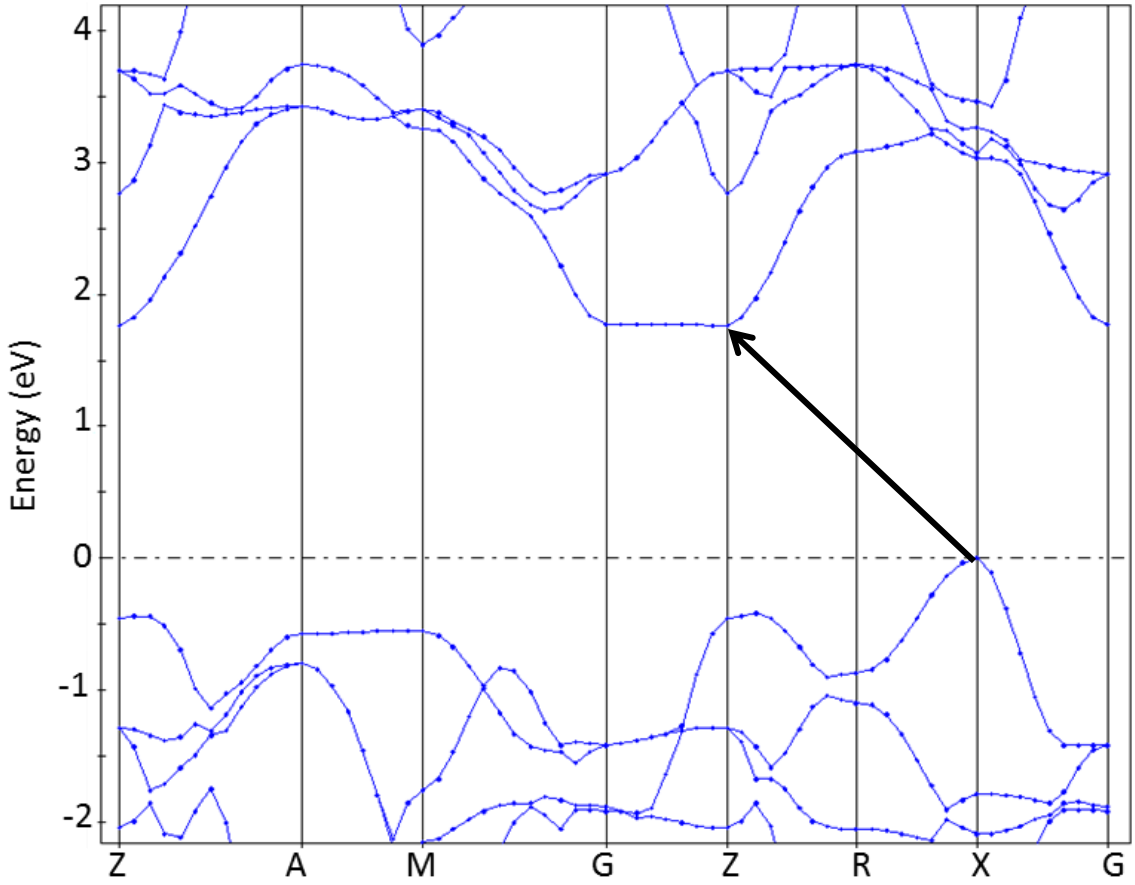

Figure 4.18: Band structure of $PbTiO_3$. The top of the valence band is at the X point and the bottom of the conduction band is at the Z point resulting in an indirect band gap.

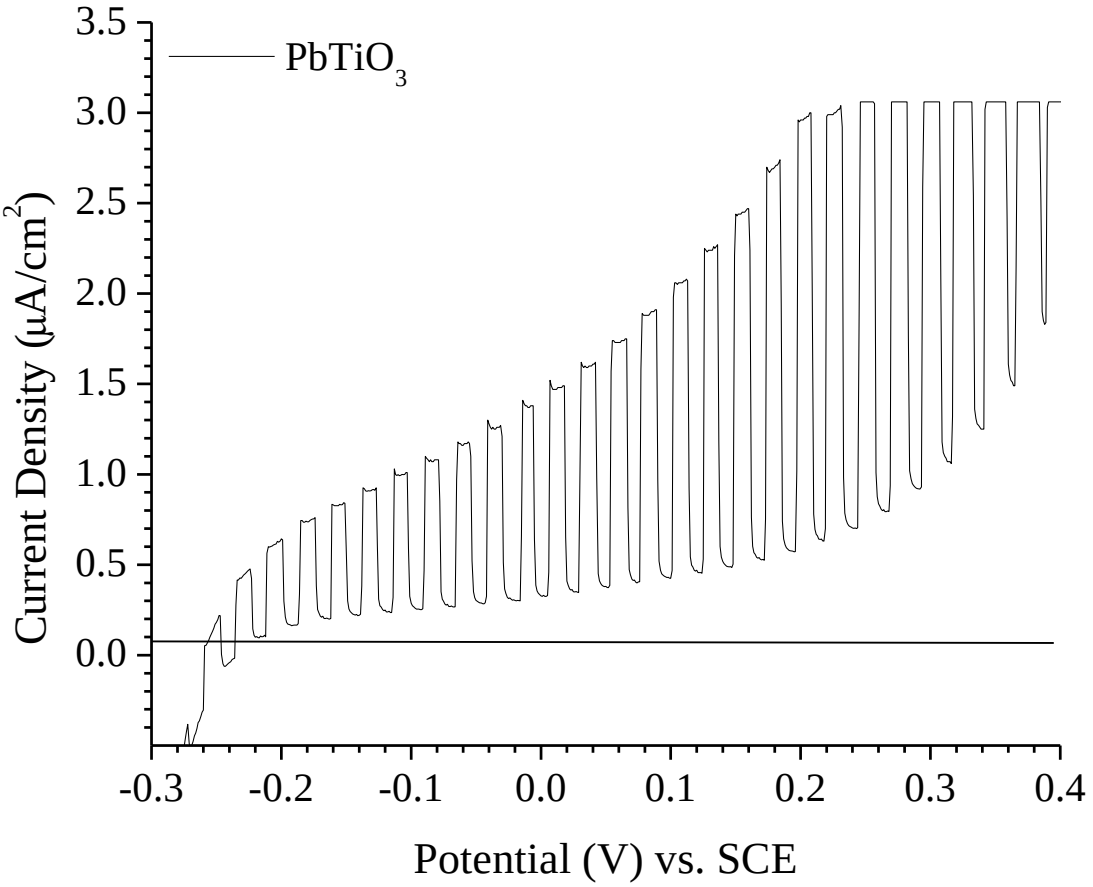

Figure 4.19: Linear sweep in 1M KOH under light chopping at 50 bpm of 600W UV-Vis irradiation of a $PbTiO_3$ film prepared by the drop-cast method and annealed at 400°C.

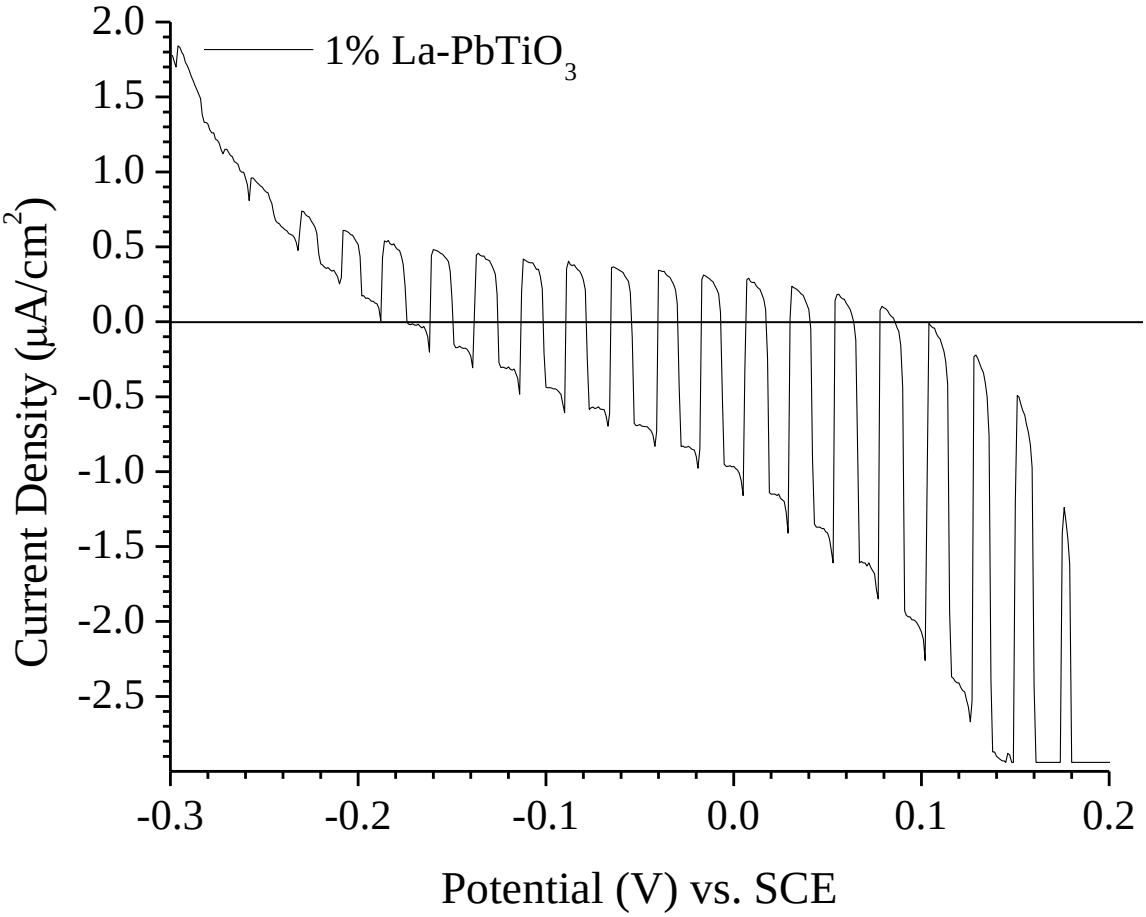

Figure 4.20: Linear sweep in 1M KOH under light chopping at 50 bpm of 600W UV-Vis irradiation of a $Pb_{0.99}La_{0.01}TiO_3$ film prepared by the drop cast method and annealed at 400°C.

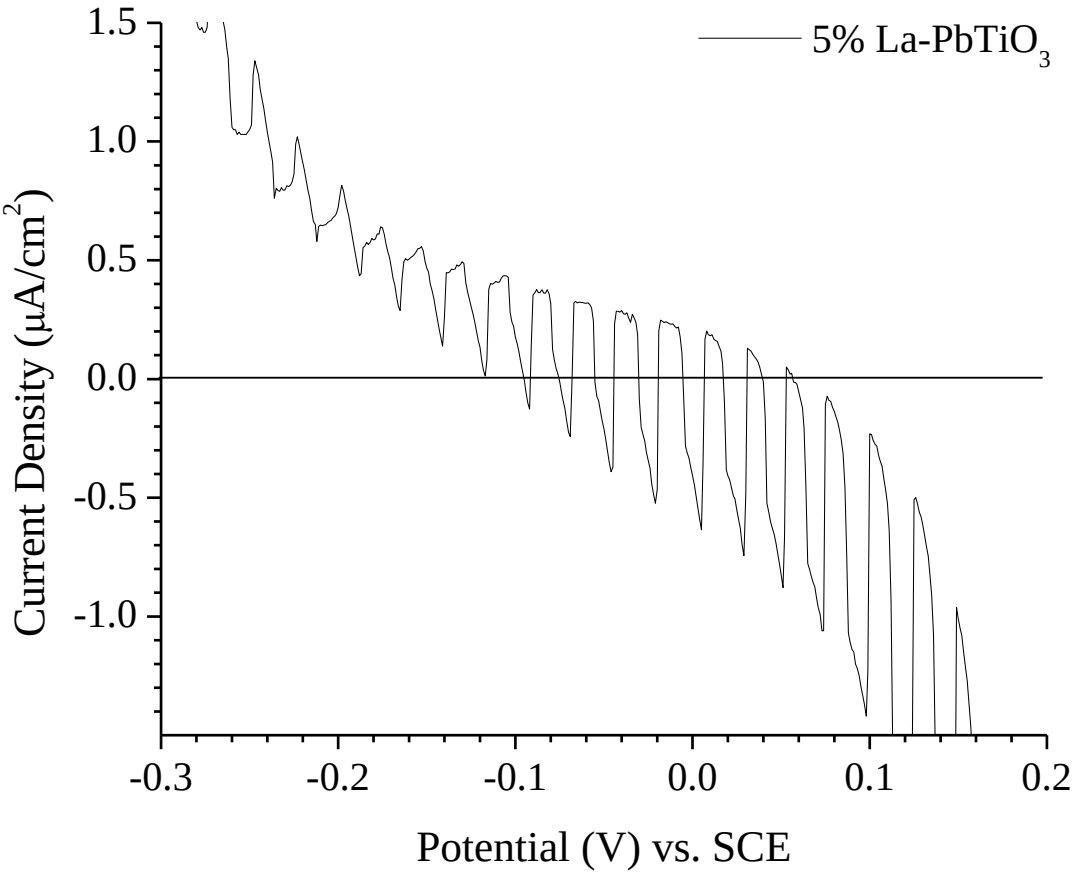

Figure 4.21: Linear sweep in 1M KOH under light chopping at 50 bpm of 600W UV-Vis irradiation of a $Pb_{0.95}La_{0.05}TiO_3$ film prepared by the drop cast method and annealed at 400°C.

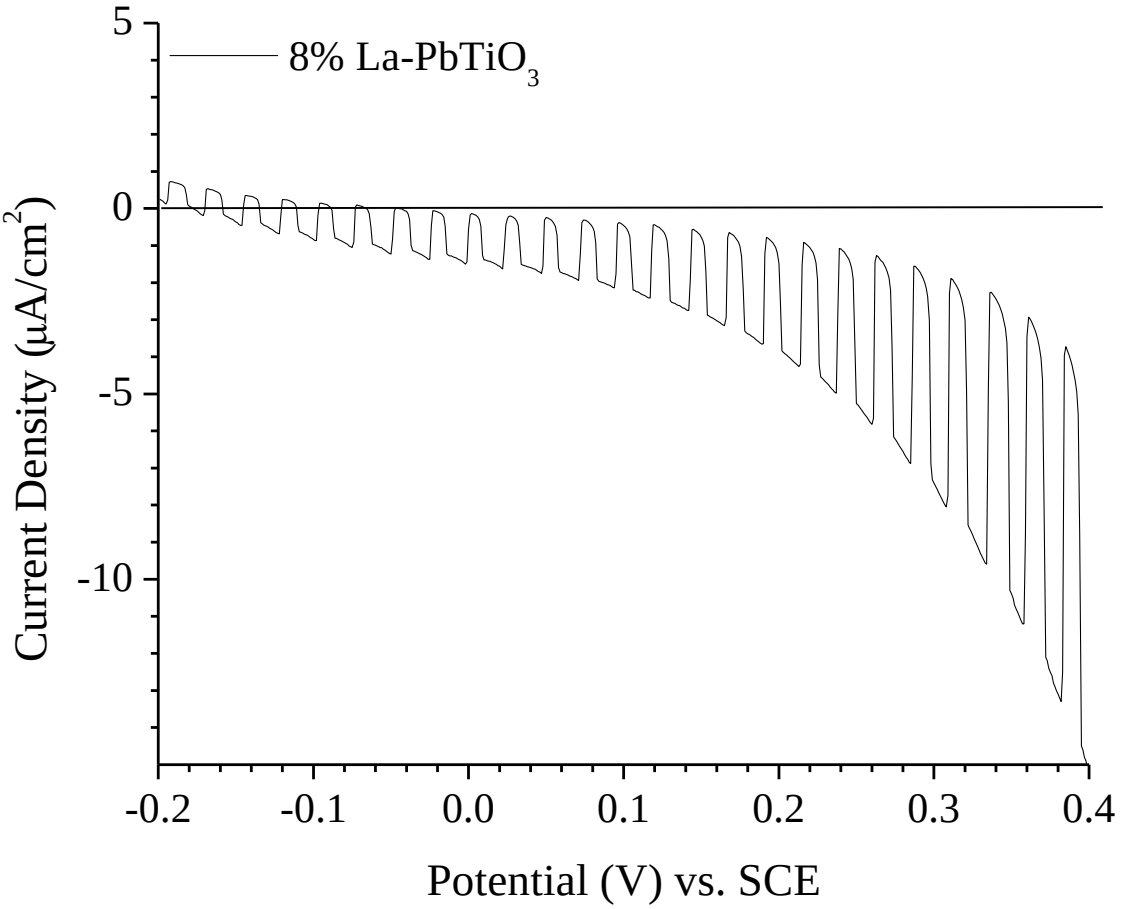

Figure 4.22: Linear sweep in 1M KOH under light chopping at 50 bpm of 600W UV-Vis irradiation of a $Pb_{0.92}La_{0.08}TiO_3$ film prepared by the drop cast method and annealed at 400°C.

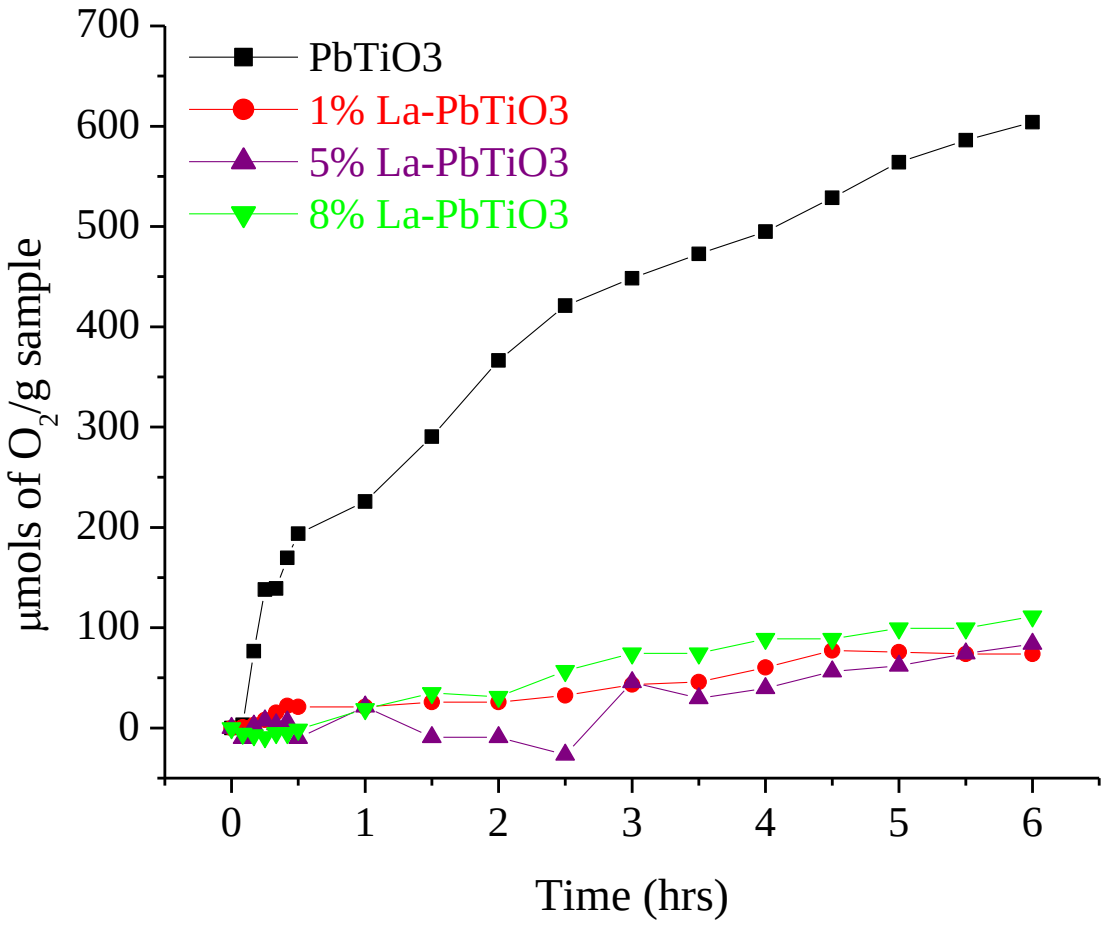

Figure 4.23: O_2 production versus time non-doped and La-doped $PbTiO_3$ in a 13.5 mmolar $AgNO_3$ solution under 1000 W UV-Vis light with stirring.

PART 3

CONCLUSIONS

The use of sunlight to provide a source of clean and renewable energy has warranted significant research in the areas of photoelectrochemistry and photocatalysis.[7,8] Two critical components of photoelectrodes and photocatalysts are visible-light absorption and charge separation and transfer.[5,6,12] Semiconducting metal-organic hybrids have shown a promising control over their structural, electronic, and optical properties leading to the investigation of many new visible-light-absorbing hybrids in past decades.[11]

Research herein focused on the synthesis of new heterometallic hybrids containing ruthenium and their electronic, optical, and physical properties. One step hydrothermal syntheses resulted in the formation of new heterometallic hybrids containing ruthenium coordination complexes. Specifically, the $[Ru(C_{10}H_8N_2)_3][NbF_6]_2$ (**I**) and $[Ru(C_{10}H_8N_2)_2(CO)Cl][V_2(C_2O_4)_3O_2(H_2O)]_{0.5} \cdot H_2O$ (**II**) hybrids were synthesized and their crystal structures were solved and refined. The lowest energy optical transitions were determined to be 2.15 eV for **I** and 2.54 eV for **II**. The onset of the optical transition in both spectra was blue shifted relative to the lowest energy optical transitions for the parent ruthenium tris-bipyridine dichloride hexahydrate ($[Ru(C_{10}H_8N_2)_3][Cl]_2 \cdot 6H_2O$) complex and parent ruthenium bis-bipyridine dichloride di-hydrate ($[Ru(C_{10}H_8N_2)_3Cl]_2 \cdot 6H_2O$) complexes. Both **I** and **II** are molecular solids with the niobium hexafluoride and vanadium oxalate complexes not linked to the ruthenium coordination complexes. The next steps in this research should focus on advancing the syntheses to form extended metal organic frameworks of ruthenium niobate and ruthenium vanadate hybrids. In addition, **I** and **II** could also be investigated as photocatalysts in future studies and compared to the parent ruthenium bipyridine complexes.

The ABO_3 perovskites, $BaSnO_3$ and $PbTiO_3$, have promising large band dispersions in their conduction bands, which indicate a high mobility of their charge carriers. Increased charge mobility is expected to assist in charge separation and transfer, based on the relationship between charge mobility and conductivity. Photoelectrochemical and photocatalytic studies have been conducted on La-doped $BaSnO_3$ and $PbTiO_3$. In this research, the syntheses of non-doped and doped $BaSnO_3$ and $PbTiO_3$ were achieved via the flux method. The effect of La-doping onto the A site was further investigated by measuring O_2 evolution activity of suspended particles and the photocurrent of thin films. Loss of photocurrent response and photocatalytic activity confirmed that La-doping into flux-prepared $BaSnO_3$ does not enhance its photoelectrochemical or photocatalytic properties. Similar results were also found for non-doped and La-doped $PbTiO_3$. The preparation of nanoparticles minimizes the effect of the dopant density on the space charge width. Yet, the La-doped $PbTiO_3$ also lost photocurrent response as well as photocatalytic activity upon doping with La^{3+} cations. However, among the doped samples there was a slight increase in photocurrent and activity, supporting the hypothesis that increasing the conductivity will increase the photoresponse. The decrease in the photoresponse and photocatalytic activity between the non-doped and La-doped $PbTiO_3$ may arise from the loss of crystallinity due to defects from La-doping.

In summary, the *n*-type doping of two ABO_3 perovskites has suggested that this approach is does not enhance their photocurrent or photocatalytic properties. If the goal is to utilize these materials as photocatalysts because of their high charge mobility character,

enhancing their photocatalytic properties might be better achieved by other approaches such as replacing the B site cation.

REFERENCES

1. Fuoco, L. C.; Flux Synthesis of Metal Oxides and Investigation of their Photoelectrochemical and Magnetic Properties, [North Carolina State University, Raleigh, North Carolina], **2012**.

2. Zhu, J.; Zäch, M.; *Current Opinion in Colloid & Interface Science* **2009**, *14*, 260-269.

3. Fahlman, B. D.; In *Semiconductors;* Springer Netherlands: Dordrecht, **2011**; pp 239-347.

4. Kudo, A.; Miseki, Y.; *Chem. Soc. Rev.* **2009**, *38*, 253.

5. Fabbri, E.; Pergolesi, D.; Traversa, E.; *Chem. Soc. Rev.* **2010**, *39*, 4355-4369.

6. Osterloh, F. E.; Parkinson, B. A.; *MRS Bull* **2011**, *36*, 17.

7. Fujishima, A.; Honda, K.; *Nature* **1972**, *238*, 37-38.

8. Grätzel, M.; *Nature* **2001**, *414*, 338-344.

9. Jayaweera, P. V. V.; Perera, A. G. U.; Tennakone, K.; *Inorg. Chem. Acta* **2008**, *361*, 707-711.

10. Osterloh, F. E.; *Chemistry of Materials* **2008**, *20*, 35-54.

11. Hagfeldt, A.; Boschloo, G.; Sun, L.; Kloo, L.; Pettersson, H.; *Chem. Rev.* **2010**, *110*, 6595-6663.

12. Krol, R.; In *Principles of Photoelectrochemical Cells;* van de Krol, R., Grätzel, M., Eds.; Springer US: **2012**; Vol. 102, pp 13-67.

13. Maeda, K.; *Journal of Photochemistry and Photobiology C: Photochemistry Reviews* **2011**, *12*, 237-268.

14. Ni, M.; Leung, M. K. H.; Leung, D. Y. C.; Sumathy, K.; *Renewable and Sustainable Energy Reviews* **2007**, *11*, 401-425.

15. Navarro, R. M.; del Valle, F.; Villoria de la Mano, J. A.; Álvarez-Galván, M. C.; Fierro, J. L. G.; In *Photocatalytic Water Splitting Under Visible-light: Concept and Catalysts Development;* Advances in Chemical Engineering; Academic Press: Vol. Volume 36, pp 111-143.

16. Murphy, A. B.; Barnes, P. R. F.; Randeniya, L. K.; Plumb, I. C.; Grey, I. E.; Horne, M. D.; Glasscock, J. A.; *Int J Hydrogen Energy* **2006**, *31*, 1999-2017.

17. Cox, P. A.; In *Transition metal oxides : an introduction to their electronic structure and properties;* Clarendon Press; Oxford University Press: Oxford; New York, **1992**.

18. Rao, C. N. R.; Subba Rao, G. V.; *Physica Status Solidi (a)* **1970**, *1*, 597-652.

19. Edited by Fierro, J. L. G.; *Metal Oxides: Chemistry and Applications;* Taylor & Francis Group: Boca Raton, FL, 2006.

20. Dutta, S.; Georgiev, I. G.; MacGillivray, L. R. In *Metal-Organic Frameworks with Photochemical Building Units;* Metal-Organic Frameworks; John Wiley & Sons, Inc.: 2010; 2010; pp 301-312.

21. James, S. L.; *Chem. Soc. Rev.* **2003**, *32*, 276-288.

22. Freitag, G.; Frustaci, D. Hybrid cathode design for an electrochemical cell. Patent US20080081259A1, **2008**, 7 pp.

23. Kuppler, R. J.; Timmons, D. J.; Fang, Q.; Li, J.; Makal, T. A.; Young, M. D.; Yuan, D.; Zhao, D.; Zhuang, W.; Zhou, H.; *Coord. Chem. Rev.* **2009**, *253*, 3042-3066.

24. Kim, H.; Chun, H.; Kim, K.; In *Selective Sorption of Gases and Vapors in Metal-Organic Frameworks;* Metal-Organic Frameworks; John Wiley & Sons, Inc.: 2010; 2010; pp 215-248.

25. Rowsell, J. L. C.; Yaghi, O. M.; *Angewandte Chemie International Edition* **2005**, *44*, 4670-4679.

26. Yan, B.; Luo, J.; Dube, P.; Sefat, A. S.; Greedan, J. E.; Maggard, P. A.; *Inorg. Chem.* **2006**, *45*, 5109-5118.

27. Kong, Z.; Weng, L.; Tan, D.; He, H.; Zhang, B.; Kong, J.; Yue, B.; *Inorg. Chem.* **2004**, *43*, 5676-5680.

28. Lin, H.; Maggard, P. A.; *Inorg. Chem.* **2007**, *46*, 1283-1290.

29. Lin, H.; Maggard, P. A.; *Inorg. Chem.* **2009**, *48*, 8940.

30. Lin, H.; Multifunctional heterometallic-oxide and -oxyfluoride hybrid solids, [North Carolina State University, United States -- North Carolina], 2010.

31. Bomben, P. G.; Robson, K. C. D.; Koivisto, B. D.; Berlinguette, C. P.; *Coord. Chem. Rev.* **2012**, *256*, 1438-1450.

32. Mikel, C.; Potvin, P. G.; *Polyhedron* **2002**, *21*, 49-54.

33. Polo, A. S.; Itokazu, M. K.; Murakami Iha, N. Y.; *Coord. Chem. Rev.* **2004**, *248*, 1343-1361.

34. Konduri, R.; Ye, H.; MacDonnell, F. M.; Serroni, S.; Campagna, S.; Rajeshwar, K. R.; *Angewandte Chemie (International ed. in English)* **2002**, *41*, 3185-3187.

35. Adams, R. D.; Trufan, E.; *Philosophical transactions. Series A, Mathematical, physical, and engineering sciences* **2010**, *368*, 1473-1493.

36. Fukuzumi, S.; Kato, S.; Suenobu, T.; *Physical chemistry chemical physics : PCCP* **2011**, *13*, 17960.

37. Ranjan, S.; Dikshit, S. K.; *Polyhedron* **1998**, *17*, 3071-3082.

38. Luo, J.; Alexander, B.; Wagner, T. R.; Maggard, P. A.; *Inorg. Chem.* **2004**, *43*, 5537-5542.

39. Beltrán, H.; Cordoncillo, E.; Escribano, P.; Sinclair, D. C.; West, A. R.; *J Am Ceram Soc.* **2004**, *87*, 2132-2134.

40. Ye, Z.; Wang, J.; Wu, Y.; Zhou, X.; Chen, F.; Xu, W.; Miao, Y.; Huang, J.; LÃ¼, J.; Zhu, L.; Zhao, B.; *Frontiers of Optoelectronics in China* **2008**, *1*, 147-150.

41. Luo, L. Investigations of Photocatalytic Activity in Heterometallic-Oxide/Organic Hybrids. North Carloina State University, 2013.

42. Borse, P. H.; Jun, H.; Choi, S. H.; Hong, S. J.; Lee, J. S.; *Applied Physics Letters* **2008**, *93*, 173103.

43. Hodes, G.; Cahen, D.; Manassen, J.; *Nature* **1976**, *260*, 312-313.

44. Kim, D. W.; Shin, S. S.; Lee, S.; Cho, I. S.; Kim, D. H.; Lee, C. W.; Jung, H. S.; Hong, K. S.; C*hemSusChem* **2013**, *6*, 449-454.

45. Guo, F.; Li, G.; Zhang, W.; *International Journal of Photoenergy*. **2010**, *2010*, 1-7.

46. Kim, H.; Kim, U.; Kim, H.; Kim, T. High Mobility in a Stable Transparent Perovskite Oxide. **2012**.

47. Sayama, K.; Nomura, A.; Zou, Z.; Abe, R.; Abe, Y.; Arakawa, H.; *Chem. Commun.* **2003**, 2908-2909.

48. Omeiri, S.; Hadjarab, B.; Bouguelia, A.; Trari, M.; *Journal of Alloys and Compounds* **2010**, *505*, 592-597.

49. Zidi, N.; Omeiri, S.; Hadjarab, B.; Bouguelia, A.; Akroun, A.; Trari, M.; *Physica B: Condensed Matter* **2010**, *405*, 3355-3359.

50. Zhang, Z.; Maggard, P. A., *J. Photochem. Photobiol. A.* **2007**, *186*, 8-13.

51. Zhang, W.; Tang, J.; Ye, J.; *Journal of Materials Research* **2011**, *22*, 1859-1871.

52. Hadjarab, B.; Bouguelia, A.; Trari, M.; *J. Phys. D* **2007**, *40*, 5833-5839.

53. Hadjarab, B.; Bouguelia, A.; Benchettara, A.; Trari, M.; *J. Alloys Compounds* **2008**, *461*, 360-366.

54. Kim, H.; Kim, U.; Kim, H.; Kim, T.; *Applied Physics Express*, V. 5, **2012**.

55. Maggard, P. A.; Boyle, P. D.; *Inorg. Chem.* **2003**, *42*, 4250.

56. Arney, D.; Watkins, T.; Maggard, P. A.; *J Am Ceram Soc* **2011**, *94*, 1483-1489.

57. Kortüm, G.; In *Reflectance spectroscopy. Principles, methods, applications;* Berlin, Heidelberg, New York, Springer, **1969**.

58. *Chemical applications of density-functional theory;* American Chemical Society: Washington, DC, **1996**.

59. Kang, H.R.; *Computational Color Technology* **2006**, 355-368.

60. Tauc, J.; Grigorovici, R.; Vancu, A.; *Phys. Status Solidi*. **1966**, *15*, 627.

61. Feng, S.; Shi, Z.; Zhang, L.; Zhao, H.; Zhang, D.; Dai, Z.; *Studies in Surface Science and Catalysis* **2001**, *135*, 3432-3439.

62. Lin, H.; Maggard, P. A.; *J. Chem. Cryst.* **2011**. *41*,1552-1559

63. Yan, B.; Capracotta, M. D.; Maggard, P. A.; *Inorg. Chem.* **2005**, *44*, 6509-6511

64. Maggard, P. A.; Yan, B.; Luo, J.; *Angewandte Chemie (International ed.in English)* **2005**, *44*, 2553-2556.

65. Maggard, P.; Kopf, A.; Stern, C.; Poeppelmeier, K.; *Cryst. Eng. Comm.* **2004**, *6*, 451-457.

66. Maggard, P. A.; Kopf, A. L.; Stern, C. L.; Poeppelmeier, K. R.; Ok, K. M.; Halasyamani, P. S.; *Inorg. Chem.* **2002**, *41*, 4852.

67. Yan, B.; Maggard, P.; *Inorg. Chem.* **2007**, *46*, 6640-6646.

68. Arney, D.; Hardy, C.; Greve, B.; Maggard, P.; *Journal of Photochemistry and Photobiology A-Chemistry.* **2010**, *214*, 54-60.

69. Lin, H.; Maggard, P. A.; *Crystal Growth & Design* **2010**, *10*, 1323-1331.

70. Biswas, M. K.; Patra, S. C.; Maity, A. N.; Ke, S.; Adhikary, N. D.; Ghosh, P.; *Inorg. Chem.* **2012**, *51*, 6687-6699.

71. Coe, B. J.; Meyer, T. J.; White, P. S. *Inorg. Chem.* **1995**, *34*, 3600-9.

72. Deacon, G. B.; Pearson, P.; Skelton, B. W.; Spiccia, L.; White, A. H.; *Acta Crystallographica. Section C, Crystal structure communications* **2003**, *59*, m537.

73. Chalmers, A. A.; Liles, D. C.; Meintjies, E.; Oosthuizen, H. E.; Pretorius, J. A.; Singleton, E.; *Journal of the Chemical Society, Chemical Communications* **1985**, 1340.

74. Chardon-Noblat, S.; Cripps, G. H.; Deronzier, A.; Field, J. S.; Gouws, S.; Haines, R. J.; Southway, F.; *Organometallics* **2001**, *20*, 1668-1675.

75. Cabeza, J. A.; Landazuri, C.; Oro, L. A.; Tiripicchio, A.; Tiripicchio-Camellini, M.; *Journal of Organometallic Chemistry* **1987**, *322*, C16-C20.

76. Soler, J.; Moldes, I.; de la Encarnacion, E.; Ros, J.; *Journal of Organometallic Chemistry*. **1999**, *580*, 108-109.

77. Vertlib, V.; Figueira, J.; Mesquita, J.; Rodrigues, J.; Nättinen, K.; Rissanen, K. A; *European Journal of Inorganic Chemistry* **2007**, *2007*, 1920-1924.

78. Pevny, F.; Di Piazza, E.; Norel, L.; Drescher, M.; Winter, R. F.; Rigaut, S.; *Organometallics* **2010**, *29*, 5912-5918.

79. Gillis, E.; Boesman, E.; *Physica Status Solidi (b)* **1966**, *14*, 337-347.

80. Moudrakovski, I. L.; Sayari, A.; Ratcliffe, C. I.; Ripmeester, J. A.; Preston, K. F.; *J. Phys. Chem.* **1994**, *98*, 10895-10900.

81. Zhang, Y.; Zhang, H.; Wang, Y.; Zhang, W. F.; *J. Phys. Chem. C* **2008**, *112*, 8553-8557.

82. Wang, H. F.; Liu, Q. Z.; Chen, F.; Gao, G. Y.; Wu, W.; Chen, X. H.; *J. Appl. Phys.* **2007**, *101*, 106105.

83. Yamashita, D.; Takefuji, S.; Tsubomoto, M.; Yamamoto, T.; *Materials Science and Engineering: B* **2010**, *173*, 33-36.

84. B'evillon, E.; Geneste, G.; Chesnaud, A.; Wang, Y.; Dezanneau, G.; *Ionics* **2008**, *14*, 293-301.

85. Upadhyay, S.; Parkash, O.; Kumar, D.; *J. Phys. D* **2004**, *37*, 1483-1491.

86. Upadhyay, S.; Parkash, O.; Kumar, D.; *Mater Lett.* **2001**, 251-255.

87. Upadhyay, S.; Kavitha, P.; *Mater Lett* **2007**, *61*, 1912-1915.

88. Ramdas, B.; Vijayaraghavan, R.; *Bull. Mater. Sci.* **2010**, *33*, 75-78.

89. Yasukawa, M.; Kono, T.; Ueda, K.; Yanagi, H.; Hosono, H.; *Materials Science and Engineering: B* **2010**, *173*, 29-32.

APPENDICES

Appendix A

Table 3.S1: Selected Bond Distances (Å) and Angles (°) for **I**.

Atom 1	**Atom 2**	**Distance**	**Intra-Polyhedral Angles**	
Ru1	N3	2.045(15)	N3 Ru1 N3	95.5(6)
	N5	2.084(16)	$N3_A$ Ru1 N5	173.4(2)
			$N3_B$ Ru1 N5	80.0(2)
			$N3_C$ Ru1 N5	89.7(2)
			N5 Ru1 N5	95.1(6)
Nb2	F1	1.861(11)	F1 Nb2 F1	90.6(5)
	F3	1.913(15)	F1 Nb2 F3	84.3(8)
			F1 Nb2 F3	89.8(6)
			F1 Nb2 F3	174.9(8)
			F3 Nb2 F3	95.3(7)
Nb3	F2	1.906(15)	F4 Nb3 F4	90.6(6)
	F4	1.865(13)	F4 Nb3 F2	86.0(6)
			F4 Nb3 F2	172.8(6)
			F4 Nb3 F2	95.8(6)
			F2 Nb3 F2	88.0(6)

Table 3.S2: Selected Bond Distances (Å) and Angles (°) for **II**.

Atom 1	**Atom 2**	**Distance**	**Intra-Polyhedral Angles**	
Ru1	Cl1	2.4170(10)	N1 Ru1 Cl01	173.16(7)
	N1	2.090(3)	N2 Ru1 Cl01	95.98(8)
	N2	2.065(2)	N3 Ru1 Cl01	86.07(7)
	N3	2.084(2)	N4 Ru1 Cl01	86.39(7)
	N4	2.130(2)	C21 Ru1 Cl01	90.63(10)
	C21	1.904(4)	N1 Ru1 N4	89.74(10)
O9	C21	1.081(4)	N2 Ru1 N1	78.64(10)
			N2 Ru1 N3	171.61(10)
			N2 Ru1 N4	93.92(9)
			N3 Ru1 N1	98.65(10)
			N3 Ru1 N4	78.07(9)
			C21 Ru1 N1	93.50(12)
			C21 Ru1 N2	89.18(11)
			C21 Ru1 N3	98.94(11)
			C21 Ru1 N4	175.91(11)
			O9 C21 Ru1	176.6(3)
V1	O1	2.018(2)	O1 V1 O5	92.40(8)
	O2	1.988(2)	O1 V1 O6	81.47(8)
	O5	2.050(2)	O1 V1 O8	162.07(10)
	O6	2.286(2)	O2 V1 O1	81.15(8)
	O7	1.599(2)	O2 V1 O5	158.48(9)
	O8	2.046(2)	O2 V1 O6	82.61(8)
O8	H8A	0.82(4)	O2 V1 O8	90.88(10)
	H8B	0.86(4)	O5 V1 O6	76.11(8)
O10	H10A	0.84(4)	O7 V1 O1	98.63(9)
	H10B	0.89(3)	O7 V1 O2	104.71(10)
			O7 V1 O5	96.53(10)
			O7 V1 O6	172.63(10)
			O7 V1 O8	98.92(11)
			O8 V1 O5	89.21(10)
			O8 V1 O6	81.60(9)

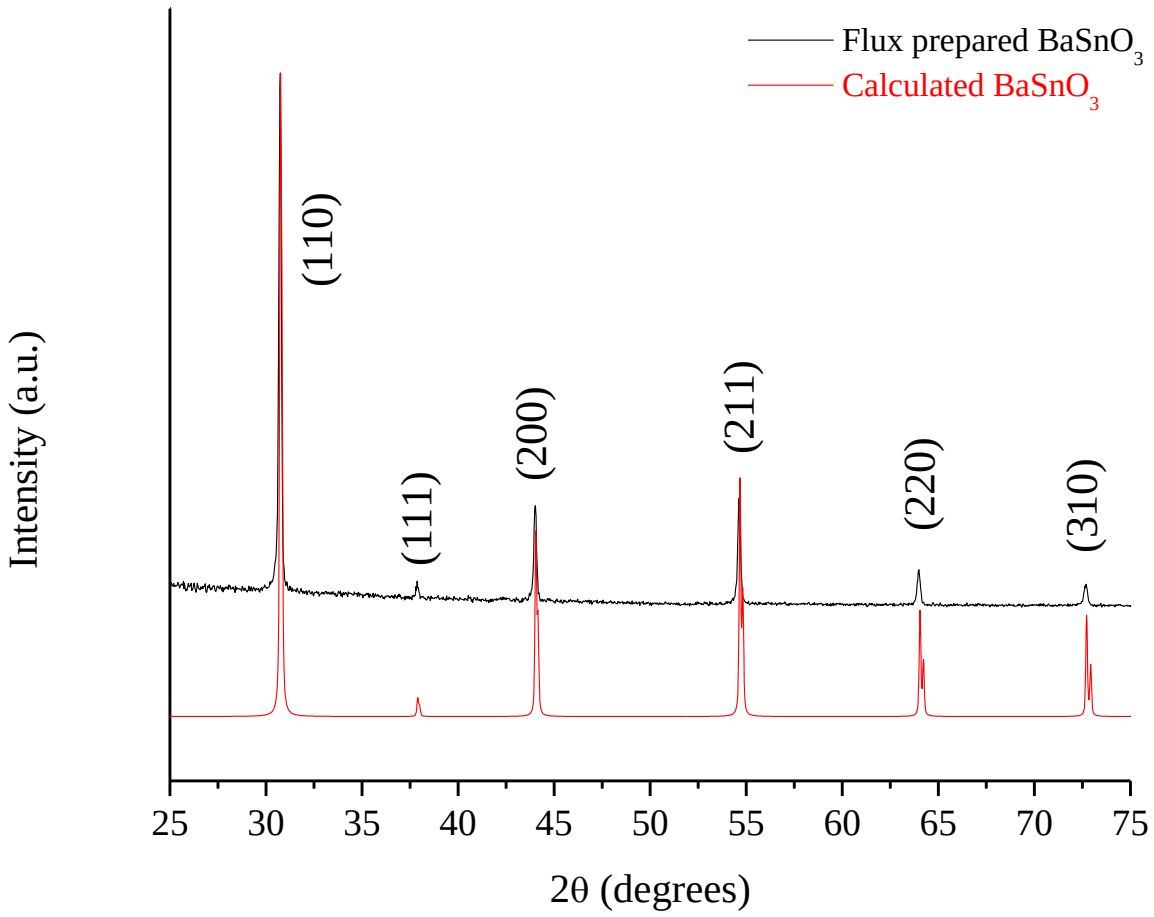

Figure 4.S1: Indexed powder X-ray diffraction pattern of $BaSnO_3$ synthesized by KOH molten flux synthesis in a 40:1 flux ratio at 800°C.

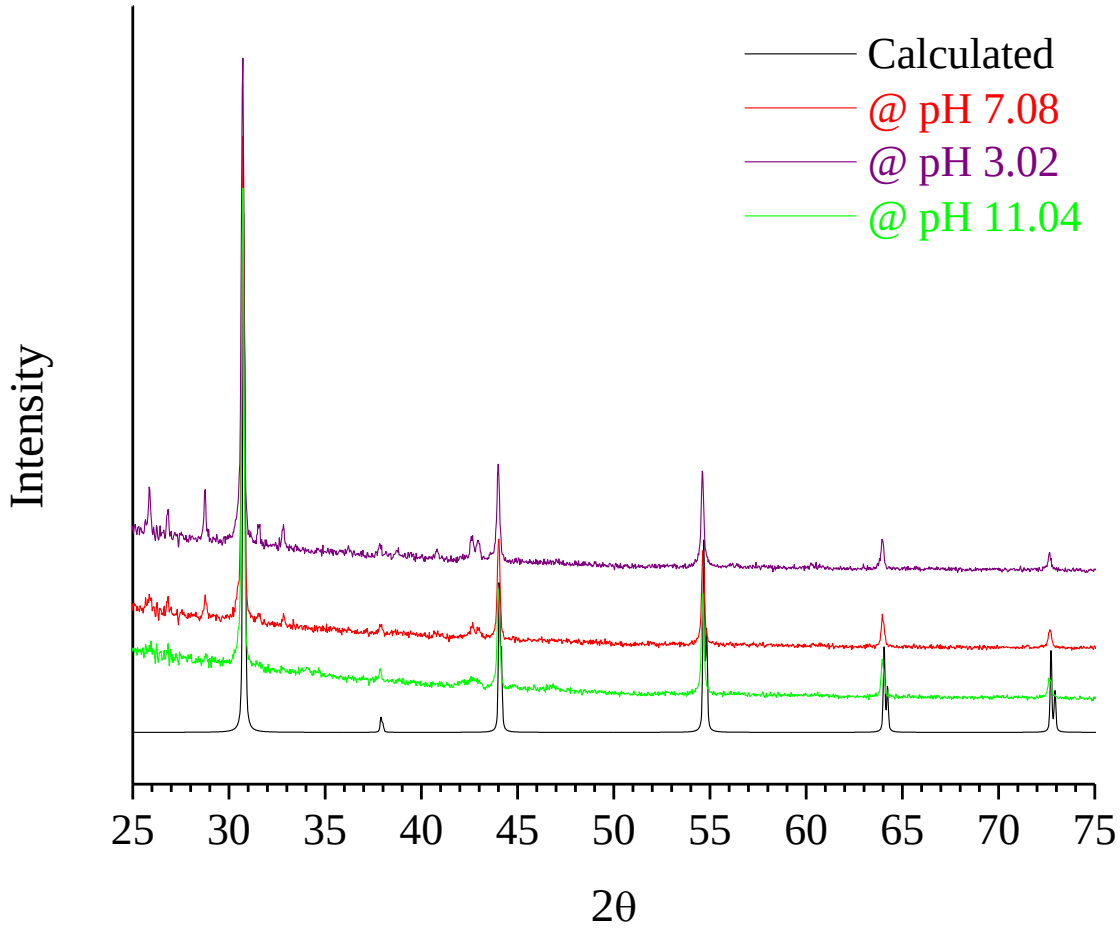

Figure 4.S2: Post PEC PXRD of $BaSnO_3$ films annealed at 500°C for 5 hours and photoelectrochemically measured at a pH of 3.02, 7.08 and 11.04 in 0.5 M Na_2SO_4 degased and bubbled with N_2.

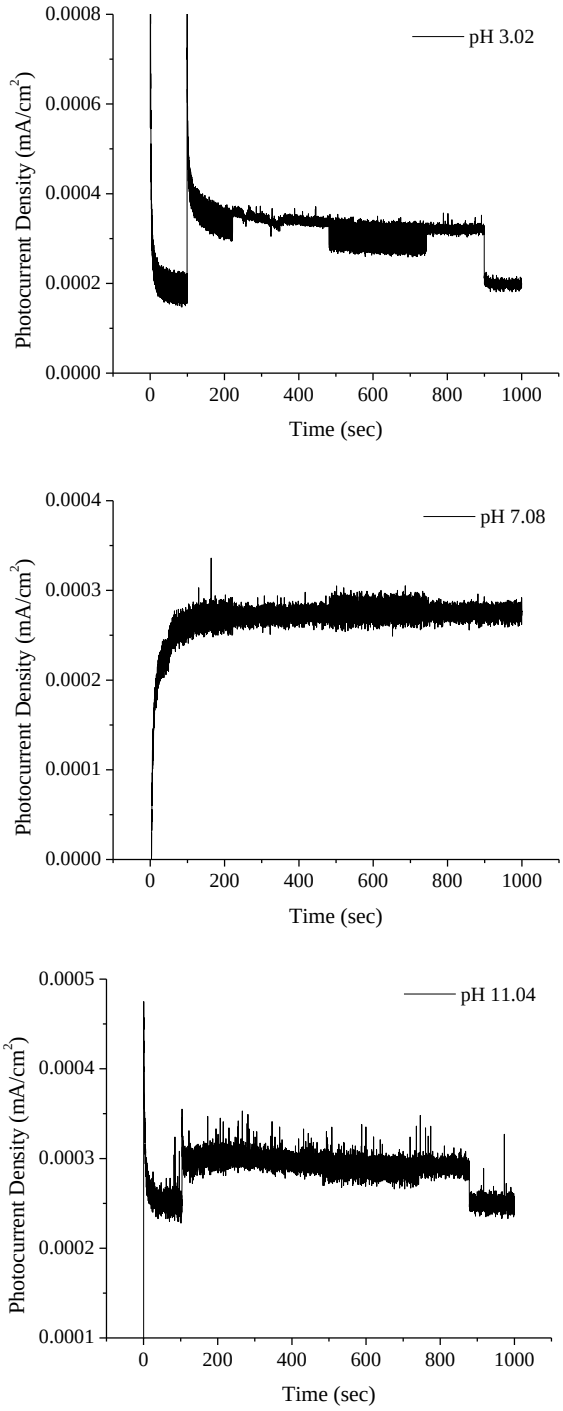

Figure 4.S3: Chronoamperometry scans of $BaSnO_3$ films in 0.5 M Na_2SO_4 at pH 3.02 (applied potential = 0.85 V), pH 7.08 (applied potential = 0.6 V), and pH 11.04 (applied potential = 0.25 V).

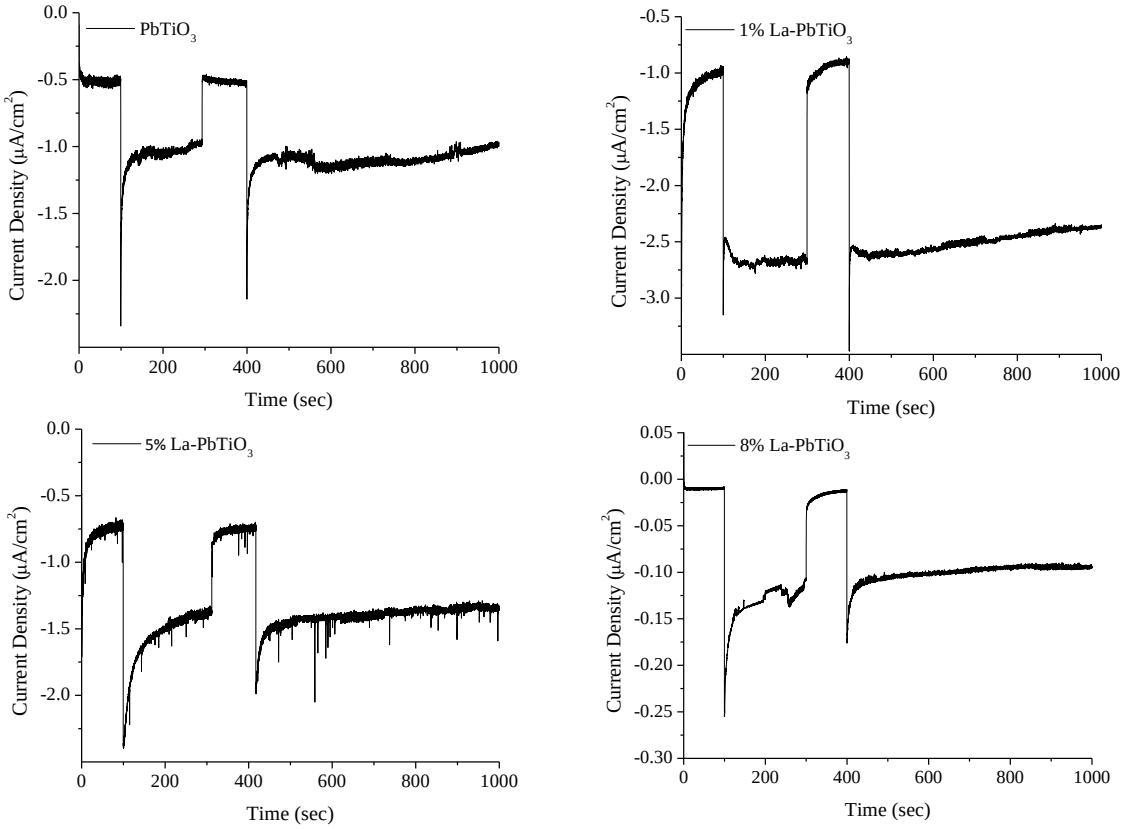

Figure 4.S4: Chronoamperometry scans of $PbTiO_3$ and $Pb_{1-x}La_xTiO_3$ films in 1M M KOH (pH ~13.25) at an applied potential of -0.2 V for $PbTiO_3$, an applied potential 0.16 V for $Pb_{0.99}La_{0.01}TiO_3$, an applied potential of 0.09 V for $Pb_{0.95}La_{0.05}TiO_3$, and an applied potential of 0.2 V for $Pb_{0.92}La_{0.08}TiO_3$.